The Hybrid Recharge Delayed Oscillator: A More Realistic El Niño Conceptual Model

Takeshi Izumo, Maxime Colin, Fei-Fei Jin, Bastien Pagli

The hybrid Recharge Delayed Oscillator: a more realistic El Niño conceptual model

Takeshi Izumo,[a,b] Maxime Colin,[c,d,e] Fei-Fei Jin,[f] and Bastien Pagli,[a]

[a]*Institut de Recherche pour le Développement (IRD), UMR241 SECOPOL (ex-EIO) laboratory, Université de la Polynésie Française (UPF), Tahiti, French Polynesia*

[b]*formerly at IRD, Sorbonne Université - CNRS- IRD- MNHN, LOCEAN Laboratory, IPSL, Paris, France*

[c]*Climate Change Research Centre, University of New South Wales, Sydney, New South Wales, Australia*

[d]*Laboratoire GEPASUD, University of French Polynesia, Tahiti, French Polynesia*

[e]*now at Leibniz Centre for Tropical Marine Research (ZMT), Bremen, Germany*

[f]*Department of Atmospheric Sciences, University of Hawai'i at Mānoa, Honolulu, HI, United States*

Submitted to Journal of Climate on March 3rd, 2023

Revised, September 6th, 2023

Revised, January 18th, 2024

Corresponding author: Takeshi Izumo, takeshi.izumo@ird.fr

ABSTRACT

The El Niño Southern Oscillation (ENSO) is the leading mode of climate interannual variability, with large socioeconomical and environmental impacts, potentially increasing with climate change. Improving its understanding may shed further light about its predictability. Here we revisit the two main conceptual models for explaining ENSO cyclic nature, namely, the Recharge Oscillator (RO) and the advective-reflective Delayed Oscillator (DO). Some previous studies have argued that these two models capture similar physical processes. Yet, we show here that they actually capture two distinct roles of ocean wave dynamics in ENSO's temperature tendency equation, using observations, reanalyses, and Climate Model Intercomparison Project (CMIP) models. The slow recharge/discharge process mostly influences central-eastern Pacific by favoring warmer equatorial undercurrent and equatorial upwelling, while the 6-month delayed advective-reflective feedback process dominates in the western-central Pacific. We thus propose a hybrid Recharge Delayed Oscillator (RDO) that combines these two distinct processes into one conceptual model, more realistic than the RO or DO alone. The RDO eigenvalues (frequency and growth rate) are highly sensitive to the relative strengths of the recharge/discharge and delayed negative feedbacks, which have distinct dependencies to mean state. Combining these two feedbacks explains most of ENSO frequency diversity among models. Thanks to the two different spatial patterns involved, the RDO can even capture ENSO spatiotemporal diversity and complexity. We also develop a fully nonlinear and seasonal RDO, even more robust and realistic, investigating each nonlinear term. The great RDO sensitivity may explain the observed and simulated richness in ENSO's characteristics and predictability.

SIGNIFICANCE STATEMENT

El Niño and La Niña events, and related southern oscillation, cause the largest year-to-year variations of earth’s climate. Yet the theories behind them are still debated, with two main conceptual models, the recharge oscillator and the delayed oscillator. Our purpose is here to address this debate by developing a more realistic theory, a hybrid Recharge Delayed Oscillator. We show how simple yet realistic it is, with equivalent contributions from the slow recharge process and from the faster delayed feedback. It even captures the observed El Niño and La Niña diversity in space and in frequency. Future studies could use the simple theoretical framework provided here to investigate the El Niño Southern Oscillation in observations, theories, climate models diagnostics and forecasts, and global warming projections.

1. Introduction

The El Niño Southern Oscillation (ENSO) is the leading mode of climate interannual variability, with large socioeconomical and environmental impacts, and with its extremes possibly increasing with global warming (e.g. Cai et al. 2021). ENSO basic amplification dynamics has been fairly well understood (e.g. Neelin 1998, Wang and Picaut 2004, Clarke 2008 reviews). Yet there are still debates on the main mechanisms at play for ENSO phase reversal and related quasi-cyclic nature, on ENSO theories / conceptual models (e.g. Graham et al. 2015; Santoso et al. 2017; Timmermann et al. 2019; Jin et al. 2020), and on how to implement ENSO diversity in these conceptual models (Fang and Mu 2018, Geng et al. 2020, Chen et al. 2022, Thual and Dewitte 2023). ENSO diversity, a continuum from extreme Eastern Pacific (EP) El Niño events to western-Central Pacific (CP) El Niño Modoki (e.g. Trenberth and Stepaniak 2001, Ashok et al 2007, Takahashi et al. 2011, Capotondi et al. 2015, 2020), and even encompassing La Niña events (Monselesan et al., submitted), is crucial to understand/forecast ENSO global impacts (e.g. Johnson and Kosaka 2016), e.g. on tropical cyclones activity in the Pacific, notably over vast French Polynesia (Vincent et al. 2011; Pagli et al., in prep.).

ENSO events usually initiate in boreal spring, develop in summer and autumn and then decay in the next spring (e.g. Bunge and Clarke 2009, Fang and Zheng 2018). They develop because of the Bjerknes positive feedback. Positive Sea Surface Temperature (SST) anomalies in the central-eastern equatorial Pacific (T_E) enhance deep atmospheric convection in the central Pacific, resulting in westerly wind stress anomalies in the western-central Pacific (τ_x; Clarke 1994). These in turn force equatorial downwelling Kelvin waves with eastward surface currents that advect the warm pool eastern edge eastward (e.g. Picaut et al. 1996; Vialard et al. 1998) and thermocline depth (h) positive anomalies towards the central-eastern equatorial Pacific, thereby reinforcing the initial SST anomalies. This positive feedback mechanism is offset by several negative instantaneous and delayed feedbacks. The delayed negative feedbacks result from oceanic dynamics: 1) a slow negative feedback related to the wind-driven slower equatorial basin adjustment to El Niño westerlies that acts to create a discharge (and a recharge in the La Niña easterlies case) of Warm Water Volume (WWV)/Oceanic Heat Content (OHC, proportional to h; e.g. Jin 1997a,b; Meinen and McPhaden 2000; Clarke 2010; Zhu et al. 2017; Izumo et al. 2019; Izumo and Colin 2022) of the southwestern and equatorial Pacific (Fig. 1b), 2) a rapid ~6-month delayed advective-reflective feedback through equatorial

84 oceanic wave reflections (e.g. Boulanger and Menkes 2001; Boulanger et al. 2004; cf. Fig. 1a
85 and section 3).
86 Two main groups of theories have emerged to explain the quasi-cyclic nature of ENSO,
87 based on the aforementioned negative oceanic feedbacks: 1) the Recharge Oscillator (RO; e.g.
88 Wyrtki 1985; Jin 1997a,b; Meinen and McPhaden 2000; Clarke et al. 2007, 2010; Thual et al.
89 2013), 2) the delayed oscillator (Suarez and Schopf 1988, Battisti and Hirst 1989) and its
90 improved version emphasizing the crucial role of Indo-Pacific warmpool eastern edge, the
91 advective-reflective Delayed Oscillator (DO; Picaut et al. 1997). An in-depth description of the
92 RO and DO is given in section 3. Other conceptual models, e.g. the unified oscillator (Wang
93 2001), have been shown to be less realistic (Graham et al. 2015).
94 Some studies question the RO and suggest that the DO is more realistic (e.g. Linz et al.
95 2014, Graham et al. 2015). Yet, the recharge/discharge process is also part of ENSO cycle,
96 both in observations and models. One reason for this "RO vs DO" debate is that RO and DO
97 have been seen as two different formal ways to represent the same wave adjustment process
98 favoring an ENSO phase reversal (e.g. Jin 1997ab; Jin and An 1999). But actually, they mainly
99 involve different physical processes with different timescales (Fig. 1). For the RO, it is the slow
100 (~1-2 years) equatorial basin adjustment (e.g. Izumo et al. 2019, their Suppl. Fig. S4)
101 influencing central-eastern Pacific SST through the thermocline feedback (e.g. Wyrtki 1985,
102 Jin 1997ab), and through heat transport changes (Izumo 2005; Ballester et al. 2015, 2016). For
103 the DO, it is the faster (~6-month) equatorial wave reflection influencing central Pacific SST
104 through the zonal advective feedback (Vialard et al. 1998). So, is it really fair to consider the
105 RO and DO as a single mechanism while they capture physical distinct processes and have
106 different impacts on the T_E tendency equation?
107 Here we show, by analyzing observations/reanalyses (section 4b) and 79 CMIP models
108 (Climate Model Intercomparison Project; section 4c), that we should keep both the recharge
109 and advective-reflective delayed feedbacks as two distinct crucial processes in the ENSO
110 temperature tendency equation, without considering them as formally identical. By keeping
111 both of them, we obtain a more physically-based and more realistic ENSO conceptual model,
112 a hybrid Recharge Delayed Oscillator (RDO; schematics in Fig. 1; derivation of its equations
113 in section 4a). We then analyze the behavior of this RDO. Section 4d explores the eigenvalues
114 dependency to parameters, within the observations and CMIP parameter space. Section 4e first
115 investigates the RDO response to stochastic forcing and related spectral response. It then shows
116 how ENSO characteristics (amplitude and spectrum) in the RDO framework are highly
117 sensitive to the relative strengths of the recharge and delayed negative feedback. Section 4f

shows that the RDO can, even its simplest form, capture some ENSO spatiotemporal diversity, if we take into account the spatial dependency of these feedbacks. Section 5 then improves the simplest RDO framework, by adding: 1) the seasonal cycles of RDO parameters (section 5a), 2) asymmetries/non-linearities, e.g. quadratic terms and a multiplicative noise (section 5b). Section 5 confirms the robustness of the RDO framework, with the non-linear seasonal RDO version being even more realistic than the linear RDO version. Finally, section 6 summarizes the results and discusses mechanisms, possible improvements of the RDO, implications and perspectives.

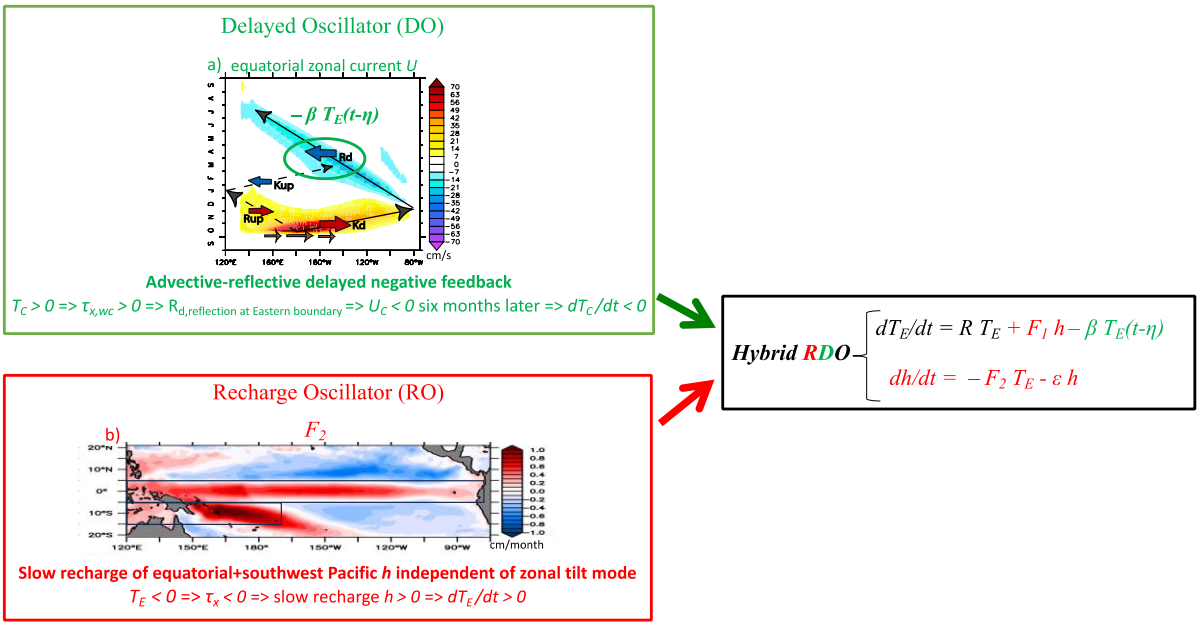

Fig. 1. Schematics of the Recharge Delayed Oscillator (RDO) principle, combining the advective-reflective Delayed Oscillator (DO; upper green; representing mainly the zonal feedback; Picaut et al. 1997) and the Recharge Oscillator (RO; bottom red; representing the slow recharge process; Jin 1997ab). a) equatorial zonal current response (in the upper oceanic layer, color shading and red/blue arrows) to a westerly pulse in early October in the western-central Pacific (brown arrows), with equatorial waves (black arrows for downwelling waves, dashed arrows for upwelling waves) and their reflections indicated schematically (in particular the downwelling Kelvin wave K_d with positive zonal current reflecting at the eastern boundary as a downwelling Rossby wave R_d with opposite negative current; see Izumo et al. 2016 for details on a similar idealized pulse experiment starting in January). **b)** slow recharge of h_{ind} (SLA independent of the fast zonal tilt mode) forced by La Niña easterly anomalies (i.e. the $-F_2T_E$ term obtained by multivariate regression in obs1; vice versa for a discharge during El Niño). T_C and U_C denote central equatorial Pacific SST and zonal current respectively; T_E denotes central-eastern Pacific SST; h is the objectively-optimized recharge index developed in Izumo and Colin (2022) study (panel b here adapted from Fig. 2h of this study), i.e. SLA (or Z20) averaged over the equatorial and southwest Pacific (black boxes in b), namely h_{ind_eq+sw} ($h_{ind\_eq+sw} \approx h_{eq+sw}$, note that the RDO robustness does not depend much of the recharge index choice; cf. section 2).

2. Data and methods

See Supplementary text S1 for a detailed description of the typical statistical methods we use, plus additional details on data, indices and validation/sensitivity tests. Note that for the non-linear seasonal version of the RDO (section 5), the scripts for obtaining the RDO parameters through multivariate linear regression fits and for running the RDO forced by red noise were developed in python language within the framework of the RO community model under development as a follow-up of the RO review by Vialard et al. (in preparation).

a. Data

For SST observations we use the following monthly datasets: Optimum Interpolation SST OISSTv2 based on *in situ* observations and satellite measurements for the recent period (November 1981-March 2022; Reynolds et al. 2002; hereafter 'obs1'); HadiSSTv1.1 SST (1870-March 2022; Rayner et al. 2003) when using longer-time-scale reanalyses. We also use GPCP monthly precipitation (Adler et al. 2003) for developing the approximated formula of sensitivity of precipitation to Relative SST.

We use SLA as a proxy for thermocline depth (e.g. 20ºC isotherm depth Z20) and Oceanic Heat Content (OHC) anomalies (e.g. Rebert et al. 1985; Gasparin and Roemmich 2017; Palanisamy et al. 2015; see Izumo and Colin 2022 for a detailed comparison of SLA, Z20 and OHC for the recharge index). SLA is advantageous because it is measured since three decades by satellites (Copernicus product; 1993-mid2021; 'obs1'), allowing a homogeneous spatiotemporal sampling. We also use longer SLA datasets for comparison and to increase the number of effective degrees of freedom: ECMWF ORAS5 oceanic reanalysis extended version (1959-2018; Zuo et al. 2019; hereafter 'obs2'; we also use its subsurface potential temperature and currents [currents only available from 1975]); even longer SLA from a historical oceanic reanalysis, SODA2.2.6 (1871-2008; Giese and Ray 2011; without subsurface assimilation to avoid spurious trends; hereafter 'hist'), required to estimate the non-linear seasonal version of the RDO, for which the number of parameters to fit strongly increases (section 5). We subtract from the SLA its 60°S-60°N global average at each time step to remove sea level rise global trend due to global warming, and we also remove any additional regional trend through a linear regression.

32 CMIP5 and 47 CMIP6 (Supplementary Table S1; Coupled Model Intercomparison Project phases 5 and 6) models are analysed here. They are the ones for which we have SST and SLA available, for the historical runs (usually 1861-2005 for CMIP5 and 1850-2015 for

CMIP6). This amounts to more than 10000 years of model data to test the validity of our hypotheses.

b. ENSO indices

For the ENSO index, T_E, we use the usual Niño3.4 region (170°W-120°W, 5°N-5°S), where the main ENSO SST variability is located in observations. We define T_E as Niño3.4 relative SST (RSST, i.e. SST minus its 20°N-20°S tropical mean; Vecchi and Soden 2007), as recommended by Izumo et al. (2020) and Van Oldenborgh et al. (2021) because atmospheric tropical deep convection interannual anomalies are rather related to RSST than to SST, notably under external forcing, i.e. anthropogenic (see also Johnson and Xie 2010; Johnson and Kosaka 2016; Williams and Patricola 2018, and Okumura 2019) or volcanic forcing (Khodri et al. 2017; Izumo et al. 2018). The deep convection threshold SST>~27-28°C (e.g. Gadgil et al. 1984) translates into RSST>~1°C, a threshold that remains valid with global warming (e.g. Johnson and Xie 2010). See Supplementary Text S3 of Izumo and Colin 2022 for an extensive discussion justifying the relevance of RSST for ENSO and RO equations. Note that using SST instead of RSST gives quasi-similar results. But it is safer to use RSST because of external forcing. T_E is normalized by its standard deviation (STD).

For the recharge index (see details and sensitivity tests in Supplementary Text S1), there has been a debate on which recharge index best measures the slow recharge/discharge process: which averaging region (e.g. western Pacific (120°E-155°W) or whole equatorial band (120°E-80°W) h_w or h_{eq} in 5°N-5°S) and which variable (SLA, Z20 (i.e. Warm Water Volume WWV) or OHC) should we use (e.g. Meinen and McPhaden 2000; Planton et al. 2018; Izumo et al. 2019) ? Izumo and Colin (2022) have thus developed a physically-unambiguous and objectively-optimized index of the ENSO slow recharge mode, out of phase with T_E (i.e. uncorrelated to T_E at lag 0 and "independent" of the fast adjustment zonal tilt mode, by regressing out from h its component linearly related to T_E approximately considered to be this fast tilt mode). Here we thus use their optimal improved index h_{ind_eq+sw}: the SLA averaged over the equatorial plus southwestern Pacific ($eq+sw$ box: equatorial box 5°N-5°S, 120°E-80°W + southwest box 5°S-15°S, 120°E-170°W), from which T_E-variability has been regressed out, to build a recharge index statistically-independent from T_E. In other words, $h_{ind\_eq+sw} = h_{eq+sw} - K\,T_E \approx h_{eq+sw}$ (as regression coefficient K is small thanks to the addition of the South West Pacific region to the equatorial band for the recharge index, e.g. 0.30 for obs2, if all indices are normalized; i.e shared variance between h_{eq+sw} and T_E only of 9%). Its advantage is that it is "orthogonal" to T_E, so it is a pure additional degree of freedom capturing the slow

recharge, without being polluted by the fast tilt mode. Also, its approximation h_{eq+sw} is simple and easy to compute.

Anyway, we would like to emphasize that the RDO robustness does not depend a lot of the recharge index choice. The RDO implementation would still be useful and robust if one were using usual indices, e.g. h_{eq} or h_w, with β, F_1 and F_2 terms still highly significant (cf. section 4). Furthermore, both β and the final correlation skill of dT_E/dt tendency equation (8) will be mathematically *exactly* the same whether or not we remove the dependent component of h index, as T_E is also one of the other variables of the multivariate regression. Therefore, if the users have a preference, they can also use the typical h_{eq} or h_w indices for the implementation of RDO. Only the overall skill of the RDO equations to represent observed temperature and recharge tendencies will be weaker than if h_{ind_eq+sw} or h_{eq+sw} is used. For the sake of simplicity and clarity of the equations, the optimal recharge index h_{ind_eq+sw} will be hereafter noted as "*h"*.

3. The two main simple ENSO conceptual models, the RO and the DO

a. The Recharge Oscillator (RO)

The RO theory (Jin 1997ab) focuses on the slow oceanic negative feedback on SST associated with wind-driven equatorial OHC variations (Meinen and McPhaden 2000), as aforementionned. It brings long oceanic memory across ENSO phases. During a La Niña, easterlies favor a slow recharge of OHC (i.e. a deepening of the thermocline depth h) in the equatorial and southwestern Pacific (Fig. 1b). The El Niño event will in turn lead to a discharge favoring a reversal to La Niña conditions, and so on.

The RO equations (Jin et al. 2020; Izumo and Colin 2022) are:

$$dT_E/dt = R_{RO}\, T_E + F_{1\_RO}\, h \qquad (4)$$

$$dh/dt = -F_2\, T_E - \varepsilon\, h \qquad (5)$$

where R_{RO} is the net effect of Bjerknes positive feedback and instantaneous negative feedback, F_{1_RO} the recharge/discharge influence on T_E, F_2 the slow recharge/discharge forced by La Niña/El Niño and ε a Newtonian damping on h. The subscript RO is added to avoid ambiguity when necessary.

Using the improved optimal recharge index $h=h_{ind\_eq+sw}$, independent of T_E (cf. section 2), ε is negligible in observations and in all CMIP models (Fig. 4b, see section 4.b). Therefore, we neglect it at first for the simplest RDO framework (linear and without seasonal cycle). This RO system of two differential equations has the form of a harmonic oscillator (Jin 1997a).

b. The Delayed Oscillator (DO)

The zonal advective-reflective delayed oscillator (DO) is based on the relatively rapid equatorial wave reflections causing a 4 to 8-month delayed negative feedback dominated by the zonal advective term (Picaut et al. 1997; Vialard et al. 1998) in the central Pacific where the coupling with atmospheric deep convection is the largest. E.g. El Niño westerlies force an equatorial downwelling Kelvin wave $K_{d,forced}$ (i.e. equatorial zonal current anomaly U' > 0 and eastward displacement of the warmpool eastern edge) reflecting at the eastern boundary into a downwelling Rossby wave $R_{d,reflection}$ (i.e. U' < 0) bringing back the edge westward half a year later (Fig. 1a) (there is also a $R_{up,forced}$ forced to the west of the westerly anomaly, propagating westward and reflecting at the western boundary as an eastward $K_{up,reflection}$ wave; e.g. Boulanger and Menkes 2001). This strong zonal advective delayed feedback favoring ENSO phase reversal is well observed, simulated and understood. Formally, it relates zonal current interannual anomalies to the evolution of zonal wind stress anomalies τ_x over the preceding months. The equatorial Pacific Ocean dynamics being quasi-linear (at intraseasonal to interannual timescales), the response to any windstress anomaly $\tau_x(t)$ with a typical ENSO wind pattern is the convolution of this $\tau_x(t)$ to the linear oceanic impulse response. Thus, the anomalies can be approximated as a "causal" filter of τ_x: ${\tau_x}^{Am}(t-t_1) - c\ {\tau_x}^{Bm}(t-t_2)$ where t_1 is ~0 to 2 months, the difference $t_2 - t_1$ is ~4 to 6 months, where the superscript, e.g. ^{Am}, stands for a A-month running mean and c varies depending on τ_x' anomaly location, and of the variable (either U, SLA or SST; cf. Izumo et al. 2016). For U_C anomalies, they are approximately proportional to the zonal wind stress anomalies 1–2 months earlier minus a fraction of the wind stress anomalies 7–8 months earlier. The first term represents the fast oceanic response, while the second one represents the delayed negative feedback associated with wave reflection at both boundaries. I.e. a realistic approximation of U_C is:

$$U_C(t) \approx A\ (\tau_x(t) - \beta_0\ \tau_x(t-\eta\ ))\qquad (6)$$

where τ_x is equatorial zonal windstress, A is a constant and β_0 is e.g. ~2/3 for U_C at 0°N, 170°W (based on Table 1 of Izumo et al. 2016 combined with the approximation ${\tau_x}^{2m} \approx {\tau_x}^{1m}$

valid for periods longer than intraseasonal). We consider the delay η to be approximately 6 months for the sake of simplicity, as it is rather well constrained by equatorial wave propagation times in a fixed basin geometry, with the main mode (first baroclinic mode) celerity well known in the equatorial Pacific. This formula is an excellent approximation of the response of the quasi-linear continuously-stratified equatorial Pacific Ocean (with a realistic coastline) to a windstress forcing with an ENSO-like spatial pattern. It is more realistic than previous approximations of U_C used in previous RO-based conceptual models.

We can combine (6) with some typical assumptions to derive a DO equation for T_C, where T_C is the SST anomaly in the central equatorial Pacific. We suppose: 1) $\tau_x \approx \mu_C T_C$ (μ_C being a coupling parameter), 2) the zonal SST gradient in the central Pacific to be its climatological value (i.e. independent of the anomaly T_C) at 1st order ($dT_C/dx \approx dT_{C\_clim}/dx \approx -C$, with $C > 0$; hence the zonal advection term is CU_C; relaxing this assumption leads to non-linear terms such as in section 5), and 3) that atmospheric fluxes can be approximated as a weak Newtonian damping (term $-r_{damp}T_C$), weaker than the Bjerknes feedback related to the 1st term in the above equation for U_C. Thus, we have, using (6):

$$dT_C/dt \approx -U_C(t)\, \mathrm{d}T_C/\mathrm{d}x(t) - r_{damp}\, T_C(t) \approx AC\mu_C\, (T_C(t) - \beta_0\, T_C(t-\eta)) - r_{damp}\, T_C(t) \quad (7.0)$$

We obtain the usual DO equation:

$$dT_C/dt = R_{DO}\, T_C(t) - \beta_{DO}\, T_C(t-\eta) \quad (7)$$

where $R_{DO} = AC\mu_C - r_{damp}$ and $\beta_{DO} = A\beta_0 C\mu_C$ are positive constants. From here onwards, we skip the notation (t) when the variable is taken at time t without delay.

4. Building the RDO model by merging the RO and DO models

a. Combining RO and DO equations

The RO captures the long-term recharge of h influencing the SST in the central-eastern Pacific. The DO captures the faster delayed advective-reflective negative feedback influencing the SST in the western-central Pacific. Knowing the importance of central Pacific SST for convection and thus zonal wind, and that the negative feedbacks involved in the DO and RO

are physically different, it thus seems relevant to keep these different feedbacks as two distinct processes combined in a hybrid « Recharge Delayed Oscillator » (RDO), whose set of equations is:

$$dT_E/dt = R\ T_E + F_1\ h - \beta\ T_E(t-\eta) \quad (8)$$

$$dh/dt = -\ F_2\ T_E - \varepsilon\ h \quad (9)$$

Equation (8) merges (4) and (7); (9) is as equation (5). Here central-eastern Pacific T_E and central Pacific T_C are merged into one variable representing a single region, the central-eastern Pacific, hereafter T_E (Niño3.4 RSST; cf. section 2), for the sake of simplicity. Even though we replace T_C by T_E, we still consider η to be about 6 months, because physically the zonal advection delayed feedback operates more on temperature "weighted" by atmospheric convection sensitivity (cf. below), i.e. more in the central Pacific than in the eastern Pacific (while the recharge thermocline feedback influences more the central-eastern Pacific; cf. following section).

This RDO simple set of equations sounds conceptually compelling. Notably it does not require the low-frequency approximation (used in Fedorov 2010 and Clarke 2010) to be valid, as the RDO takes into account the two main "fast" wave processes, the fast mode adjustment, and the zonal-advective delayed negative feedback.

b. Confirming the RDO through observations/reanalyses

We now want to verify empirically that this RDO set of equations is justified and statistically grounded, in observations as well as in the 79 CMIP models.

First, we verify that separating the zonal-advective delayed feedback and the recharge process through equation (8) makes sense. I.e. that $+F_1 h$ and $-\beta T_E(t-\eta)$ represent two distinct physical processes. We do a multivariate linear regression for an equation similar to equation (8), but for the tendency of temperature $T(x,y,t)$ anywhere in the tropical Pacific:

$$\partial T(x,y,t)/\partial t = R(x,y)\ T_E + F_1(x,y)\ h - \beta(x,y)\ T_E(t-\eta) \quad (8.1)$$

The regression quantifies the contributions of $-\beta(x,y)T_E(t-\eta)$ and $F_1(x,y)h$ terms to $T(x,y,t)$ tendency at each grid point. Fig. 2ab compares their spatial patterns in the tropical Pacific, that are indeed quite different (orthogonal). Indeed, we see that the $-\beta T_E(t-\eta)$ contribution is stronger in the western-central Pacific, especially near the warm pool eastern edge, where the

zonal advection term dominates. It confirms that $-\beta T_E(t-\eta)$ represents the zonal advective-reflective delayed negative feedback. Conversely, the recharge term $F_1 h$ is larger in the eastern Pacific as expected, as the thermocline feedback term is stronger there (i.e. the recharge/discharge process is more important for EP than for CP El Niño events; e.g. Hasegawa et al. 2006; Kug et al. 2009, 2010; McPhaden 2012; Capotondi 2013; Ren and Jin 2013). Fig. 3a compares more quantitatively their values along the equator. The contribution of $-\beta T_E(t-\eta)$ is larger than that of $F_1 h$ in the western-central Pacific (around Niño4 region), while the contribution of $F_1 h$ is the largest in the central eastern region (from ~150°W, the western boundary of Niño3 region), for both obs1 and obs2 datasets (that are consistent, with differences not significant at the 90% level, cf. Suppl. Fig. S1; while β and F_1 differences are statistically significant). Note that $R(x,y,t)$ is, as β, larger in ~Niño4 region (Suppl. Fig. S1d, likely because of the largest positive Bjerknes feedback there). R is however only about one third of β there. The correlation skill of equation (8.1) is high east of the dateline, being at its largest around Niño3.4 region (Suppl. Fig. S1d), where β and F_1 roles add up. This also confirms that focusing on Niño3.4 region is a good approximation.

Considering only RSST tendency (Fig. 2ab), we could think that the recharge term dominates the delayed term. Yet, in terms of feedback to deep convection/precipitation/windstress, the deep convection (the primary contributor to precipitation in the Tropics) sensitivity to RSST anomalies is larger in the western Pacific warmpool region, where climatological RSST is larger, than in the central-eastern cold tongue region (e.g. He et al. 2018 study had estimated a formula for the precipitation sensitivity to SST, $P(SST)$). To illustrate this, we can use a simple exponential formula we have developed as an approximation of the precipitation sensitivity to local RSST, $P(RSST)$ (Appendix Fig. A1):

$$P(RSST) = 2\, e^{0.56 RSST} \quad (8.2)$$

Where RSST is the total RSST field (including both climatology and anomaly, i.e. $RSST_{clim}$+RSST'). The constant 0.56 is taken from the term representing the effect of RSST on deep convection in Tippett et al. (2011) cyclogenesis index (efficient at describing the cyclogenesis seasonal cycle at the global scale; Menkes et al. 2012). The factor 2 (in mm day^{-1}) is a crude fit to the scatterplot of $Precip_{clim}$ to $RSST_{clim}$ in the equatorial Pacific (this factor will anyway not influence the relative contributions to $dP(RSST)/dt$ of $-\beta T_E(t-\eta)$ and $F_1 h$ that are our focus here). Fig. 2cd is as Fig. 2ab, but for $dP(RSST)/dt$. The contribution to convective

precipitation tendency of $-\beta T_E(t-\eta)$ has actually, in the western-central Pacific, an almost similar amplitude to the contribution of $F_1 h$. Note that these estimated contributions to local precipitation will be then amplified by the convergence feedback (Conditional Instability of the Second Kind; CISK), notably for strong El Niño events in the central-eastern Pacific (Srinivas et al. 2022). To conclude, the $-\beta T_E(t-\eta)$ term can force large tendencies in precipitation and related equatorial zonal windstress, crucial for the ocean-atmosphere coupling. Hence adding the $-\beta T_E(t-\eta)$ term to the $\partial T(x,y,t)/\partial t$ equation can make the conceptual model significantly more realistic.

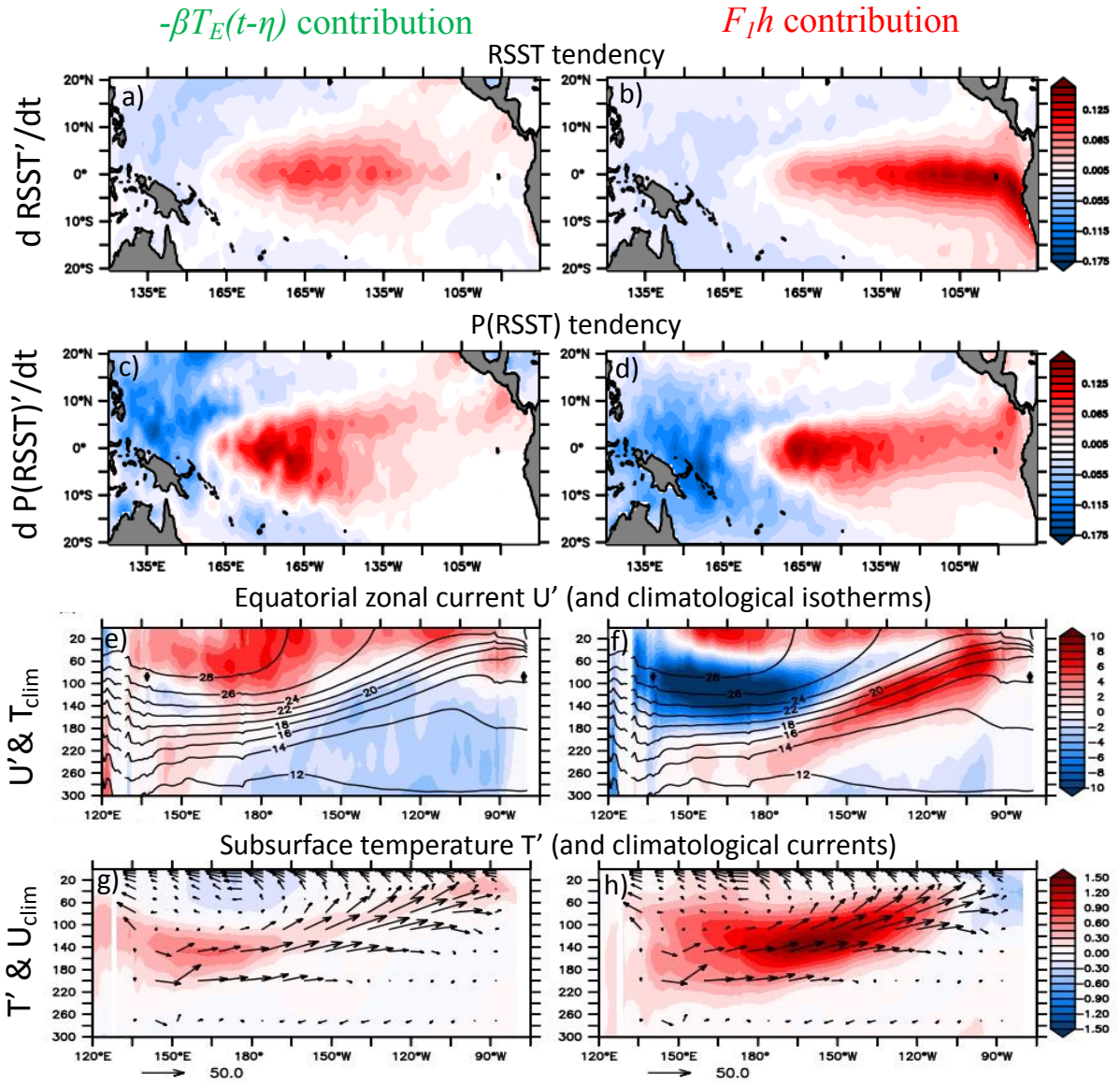

Fig. 2. Distinct physical processes represented by $-\beta T_E(t-\eta)$ and $F_1 h$ terms in RDO, and related ENSO spatiotemporal diversity captured by the RDO. a and **b)** contributions of respectively $-\beta(x,y)T_E(t-\eta)$ and $F_1(x,y)h(t)$ to $\partial T(x,y,t)/\partial$t(t) in Equation 8.1 (i.e. the regression coefficients $\beta(x,y)$ and $F_1(x,y)$ for normalized T_E and h, i.e. unit in °C.month^{-1} per STD of T_E or h) for obs2. By reconstructing $T(x,y,t)$ from these patterns, the RDO can simulate part of ENSO spatial and spectral diversity (cf. section 4f). **c** and **d)** as a and b, but for the expected response of deep convection/precipitation to RSST tendency shown in a and b (mm day^{-1}

month^{-1}), more sensitive to RSST anomalies in the western Pacific warmpool than in the central-eastern cold tongue region (based on equation 8.2: $P(RSST)= 2\ e^{0.56RSST}$). Lower panels show the oceanic mechanisms behind $-\beta T_E(t-\eta)$ and $F_1 h$ contributions to $\partial T(x,y,t)/\partial t$. **e** and **f** are as a and b, but for equatorial (2ºN-2ºS average) subsurface zonal current anomaly U' (color, cm/s), with climatological isotherms T_{clim} overlayed (black contours, ºC). **g** and **h**) as a and b, but for subsurface potential temperature anomaly T' (color, ºC), with climatological zonal and vertical currents U_{clim} and W_{clim} overlayed (black vectors, cm s^{-1}).

To understand the oceanic mechanisms behind $-\beta(x,y)T_E(t-\eta)$ and $F_1(x,y)h(t)$ contributions to $\partial T(x,y,t)/\partial t$, remember that the temperature tendency of the oceanic mixed layer is firstly due to heat advection (see its full decomposition in Supplementary Figures S2 an), with surface fluxes acting to damp interannual SST anomalies. So as to understand heat advection anomalies, Fig. 2 lower panels show equatorial subsurface zonal current anomaly U', with climatological isotherms T_{clim} overlayed, as well as subsurface potential temperature anomaly T', with climatological currents U_{clim} and W_{clim} overlayed.

The $-\beta T_E(t-\eta)$ contribution is firstly through a large positive U' anomaly in the upper layer. U' is maximal near the dateline (up to 6 cm s^{-1} per STD of $T_E(t-\eta)$; Fig. 2e), consistent with the timing of the westward propagation of the equatorial upwelling Rossby wave forced by easterly anomalies 6 months earlier (in the case of a prior La Niña with negative T_E and easterlies; Fig. 1a was shown for the opposite westerly case). This eastward current anomaly U' advects the negative climatological zonal temperature gradient $\partial T_{clim}/\partial x$, i.e. $-U'\partial T_{clim}/\partial x$ (Suppl. Fig. S3c), favoring a warming of the oceanic mixed layer in the central Pacific (of up to 0.15K month^{-1}, i.e. about 1K in half a year, per STD of $T_E(t-\eta)$; Suppl. Fig. S2c). The T' anomalies related to $-\beta T_E(t-\eta)$ are conversely weak near the surface (about 0.2K per STD of $T_E(t-\eta)$; Fig. 2g) and have a secondary role (Suppl. Fig. S3a) in the heat zonal advection of the mixed layer (and at the subsurface, they are much weaker than those related to $F_1 h$; see also Fig. 3c). This analysis confirms that $-\beta T_E(t-\eta)$ contribution is firstly through zonal advection in the central Pacific, i.e. $-\beta T_E(t-\eta)$ represents the zonal advective-reflective delayed negative feedback.

The recharge influence $+F_1 h$ represents a different physical process. $F_1 h$ influence is through warmer EUC and upwelling because of the warm subsurface anomaly in the central-eastern Pacific due to the recharge and related deeper thermocline. h recharge favors a large subsurface warm anomaly in the heart of the Equatorial UnderCurrent (EUC shallower in the east, like the thermocline, from ~150m at 180ºE to ~100m at 130ºW). This warm T_{EUC}' anomaly, partly due to the deeper thermocline (cf. Izumo 2003, 2005), will be advected by the climatological EUC, i.e. a positive term $-U_{clim}\ \partial T'/\partial x$ (Suppl. Fig. S3b). It is also within the climatological equatorial upwelling, i.e. $-W_{clim}\ \partial T'/\partial z$ (Suppl. Fig. S3f). I.e. the EUC will bring

warmer waters to the central-eastern Pacific, where they will be upwelled to the mixed layer by the climatological upwelling, favoring an overall warming tendency of the mixed layer of the central-eastern equatorial Pacific (Suppl. Fig. S2b). Note that there are secondary roles of: 1) an increase of the deepest part of the EUC in the east (because of increased zonal gradient of thermocline since the recharge is more in the western-central than in the eastern Pacific), i.e. $-U' \partial T_{clim}/\partial x$ (Suppl. Fig. S3d), 2) an upwelling reduction in the extreme east, east of ~100ºW, i.e. $-W' \partial T_{clim}/\partial z$ (Suppl. Fig. S3h).

To better understand the origin of this warm subsurface anomaly, we have to remember that the EUC is part of a large-scale 3D circulation. It is fed by the north and south meridional pycnocline convergences, at their largest in the western Pacific. They are the lower branches of the shallow SubTropical/Tropical Cells (STCs/TCs; McCreary et al. 1992; McCreary and Lu 1994; Zeller et al. 2019, 2021). The south convergence is climatologically two times larger than the north one (because of the potential vorticity barrier in the north) and is the first origin of EUC waters (Blanke and Raynaud 1997; Stellema et al. 2022). Hence, the h recharge associated to deeper thermocline in the equatorial and southwest Pacific favors warmer transport-weighted temperatures of the meridional pycnocline convergences, notably the dominant south convergence related to southwest Pacific recharge, thereby feeding the EUC with warmer waters (Izumo 2003, 2005; Ballester et al. 2015, 2016). Note by the way that the north-south asymmetry in the convergence further justifies the use of the asymmetric recharge index h_{eq+sw}.

Fig. 3bc summarizes the distinct dominant oceanic processes for the delayed feedback (green line) and recharge term (red). The delayed feedback dominates for U' in the west and central Pacific upper layer, i.e. for zonal advection $-U' \partial T_{clim}/\partial x$. The recharge term dominates for the subsurface temperature anomaly T' advected by the mean 3D circulation, i.e. by the climatological EUC through $-U_{clim} \partial T'/\partial x$, and by climatological upwelling through $-W_{clim} \partial T'/\partial z$, in most of the equatorial Pacific.

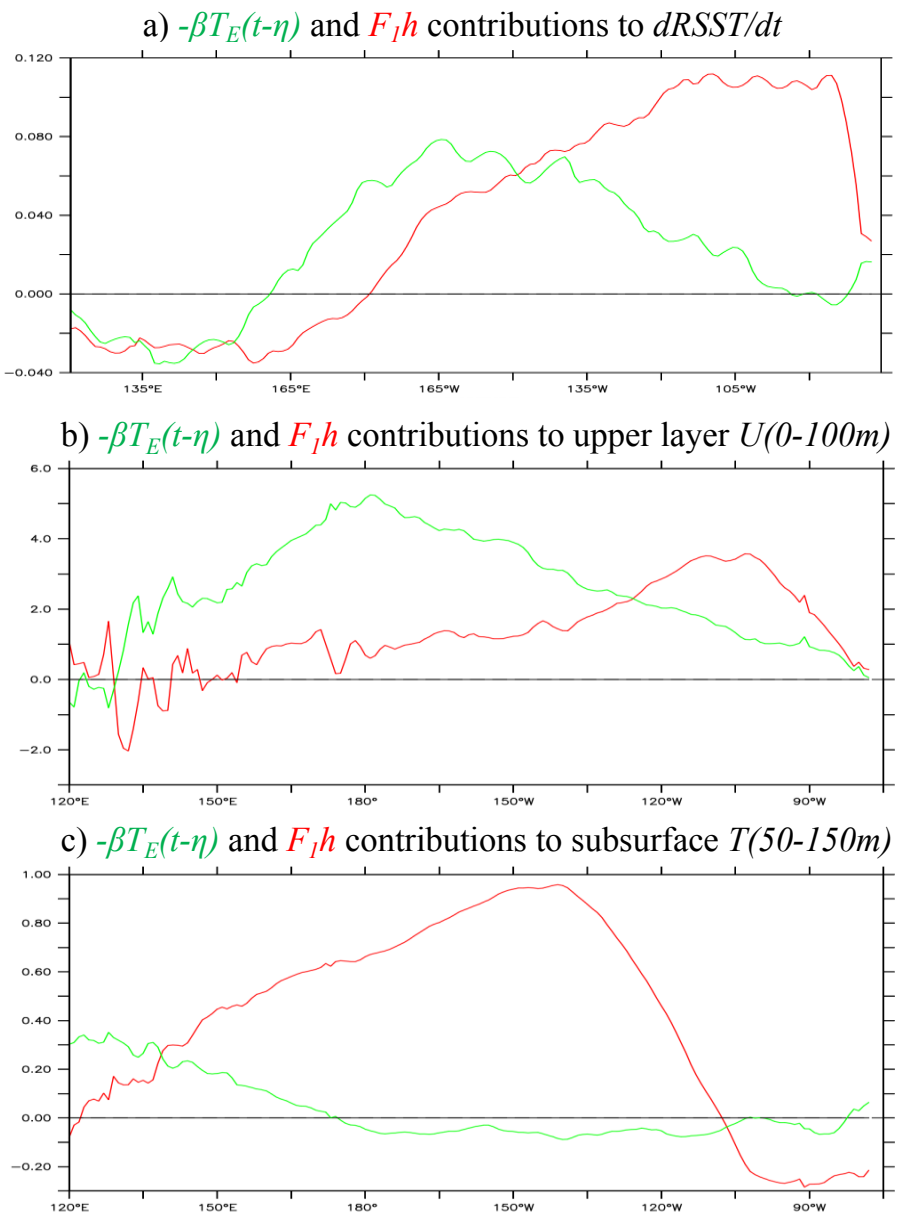

Fig. 3. Equatorial contributions of delayed feedback $-\beta T_E(t-\eta)$ (green) and of recharge term $F_I h$ (red). **a)** as Fig. 2ab for RSST tendency, but for the 5ºN-5ºS average. **b)** as a but for upper layer (0-100m average) zonal current. **c)** as a but for subsurface potential temperature (50-150m average).

Overall, these analyses confirm from observations/reanalysis that this RDO is physically-grounded, the two terms $-\beta T_E(t-\eta)$ and $F_I h$ being both important and representing distinct physical processes. It is hence more physical to distinguish these two terms, equation (8) being one reasonable way to conceptualize them. Furthermore, we will later on show that the different spatial patterns of β and F_I seen in Fig. 2ab allow the RDO to capture partly the ENSO spatiotemporal diversity in equatorial Pacific $T(x,y,t)$. But for now, we will firstly analyze the RDO in its simplest form, focusing on spatially-averaged Niño3.4 RSST, namely $T_E(t)$.

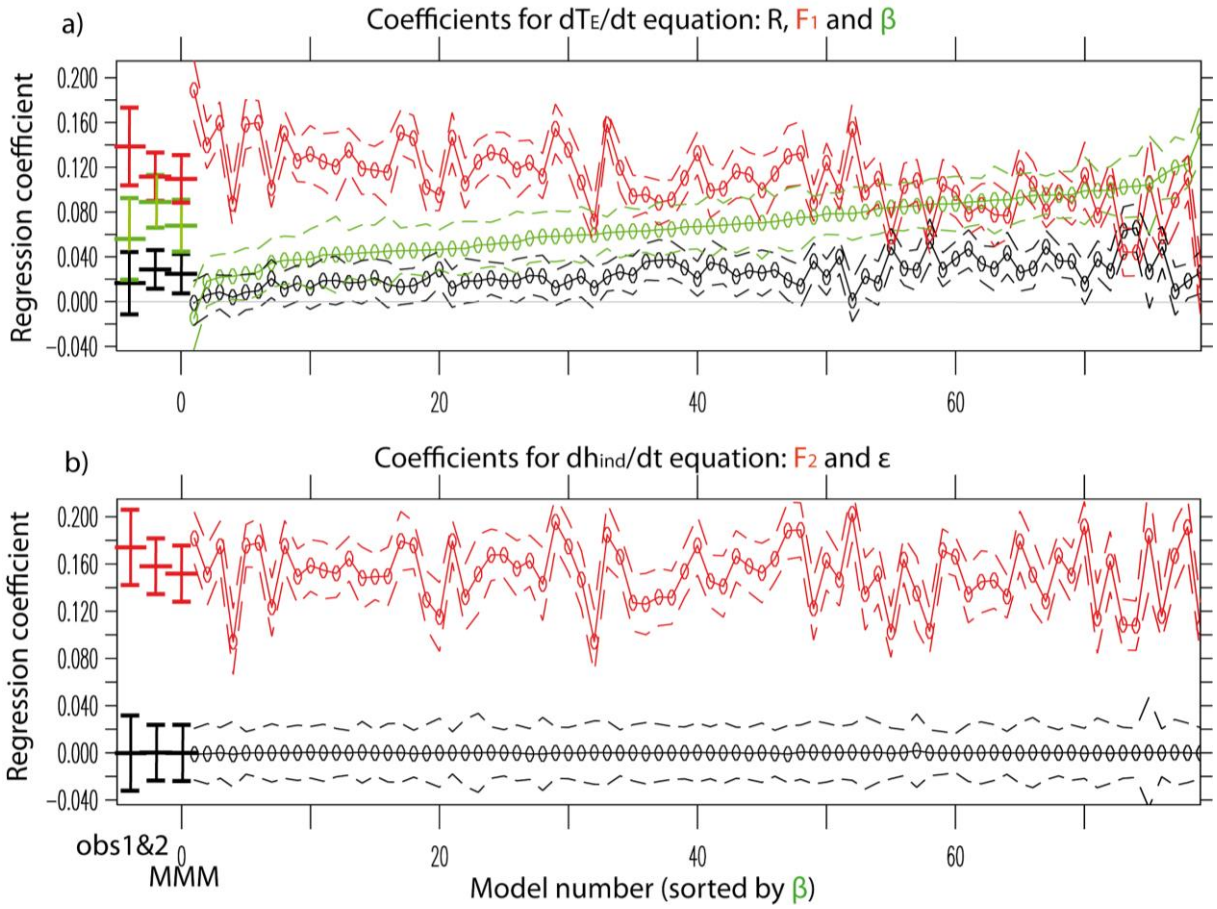

Fig. 4. Significance of the RDO coefficients in observations and CMIP. a) coefficients R (black), F_1 (red) and β (green) of the regression of dT_E/dt onto normalized $T_E(t)$, h(t) and $T_E(t-\eta)$ (cf. Equation 8) for the 79 CMIP models sorted by β (numbers 1 to 79 on x-axis). **b)** coefficients F_2 (red) and ε (black) of the regression of dh/dt onto h(t) and $T_E(t)$ (cf. Equation 5). Three thick error bars from the left respectively show obs1, obs2 and Multi-Model Mean (MME). T_E and h are normalized so that regression coefficients (in $month^{-1}$) can be compared, whatever the model's ENSO amplitude. 90% confidence intervals are shown as dashes, and for observations and MMM as marks.

A 2nd way of confirming the relevance of the RDO equation (8) is to compute the coefficients *R*, F_1 and β obtained from the multivariate linear regression of dT_E/dt onto $T_E(t)$, $h(t)$ and $T_E(t-\eta)$ for observations (and in the following section for CMIP models), now focusing on the tendency of spatially-averaged T_E, as shown in the very left of Fig. 4a for observations. The most striking result is that F_1 and β are *both* highly-significantly positive in obs1 and obs2 (at the 95% level). Therefore, both need to be taken into account, and cannot be neglected in Equation (8). Consistently, observed *h* and $T_E(t-\eta)$ have more than half (~60%) of unshared variance, in agreement with the fact that they firstly represent different physical processes.

c. Confirming the RDO through CMIP multi-model database; mean state influence

Accordingly, the RDO equation is also relevant for most CMIP models, with F_1 and β being both significantly positive in almost all the CMIP models (Fig. 4). In the following, we write variable X = X1[X2]{X3} with X1 for values obtained with 'obs1' (OISST and satellite SLA), X2 for 'obs2' (HadiSST and ORAS5 SLA) and X3 for Multi Model Mean (MMM) of CMIP5 and CMIP6 historical runs. CMIP MMM values lie within observational uncertainties: (F_1,β) = (0.14±0.03,0.06±0.04) [0.11±0.02,0.09±0.02] month^{-1} for observations and {0.11±0.02,0.07±0.02} for CMIP (similar values for CMIP5 and CMIP6 MMM). Note that the relative strengths of F_1 and β can also depend of the period used (consistent with the fact that the dominant ENSO flavor may have changed with time). E.g. longer obs2 can be compared to obs1 on their 26-yr long overlapping period, 1993-2018. It gives (F_1,β) = [0.13±0.02,0.06±0.02] month^{-1}, almost similar to obs1, with F_1 larger than β. While obs2 on the 26-yr earlier period 1959-1984 gives (F_1,β) = [0.09±0.02,0.10±0.02] month^{-1}, with conversely F_1 weaker than β (possibly because of higher-frequency ENSO during that period; cf. section 4; such decadal changes could partly explain the changes in observed WWV/T_E lag-relationship shown by McPhaden 2012 and confirmed by Crespo et al. 2022). The R coefficient is weaker, R = 0.02±0.03 [0.03±0.02]{0.02±0.02} month^{-1}, but is still significantly positive at the 90% level in the majority of CMIP models in this new RDO framework, contrary to R_{RO} that is not significantly different from zero in the pure RO framework. The correlation skill of the RDO dT_E/dt equation (8) is highly significant (r_{Te} =0.71[0.68]{0.64}), also confirming the RDO relevance. The Steiger's test (on the difference between these two dependent correlations from a single sample; note that the correlations are overlapping, sharing one variable in common) allows us to compute the significance of the improvement of the skill (and of its square, i.e. explained variance) in obs1[obs2]: from RO to RDO, this significance is 84%[97%] (explained variance increases from 48% to 51% [41% to 46%]), and from DO to RDO, it is 99%[99%] (explained variance increases from 34% to 51% [35% to 46%]). For CMIP MMM, the improvement is even more significant statistically, given the much longer timeseries: the explained variance increases by ~10% from RO to RDO (from 34 to 38%) and by ~20% from DO to RDO (from 29% to 38%). Note that, in the most realistic version of the RDO, the non-linear seasonal RDO developed later, the improvement is even much larger (section 5).

Interestingly, there is a large CMIP inter-model diversity in the relative strengths of the coefficients F_1 and β, larger than for R (Fig. 4a). The models (sorted by the amplitude of β in Fig. 4) that have a large F_1 tend to have a weak β, and vice versa (inter-model correlation = -

0.69). R is positively correlated to β (0.59) and negatively correlated to F_1 (-0.75). This large diversity of the parameters is likely related to the diversity of spectral, spatial and amplitude (related to growth rate) characteristics of ENSO and of Pacific mean state (cf. below) among CMIP models.

Fig. 4b similarly shows the coefficients F_2 and ε for the regression of *dh/dt* onto $T_E(t)$ and *h(t)*. F_2 is highly significant in all observations and models, F_2 = 0.17±0.03 [0.16±0.02]{0.15±0.02} month^{-1} and more consistent in amplitude among CMIP than F_1 and β, with a weaker inter-model diversity (~ ±30% of MMM value) positively correlated with F_1 (inter-model correlation = 0.79). As in observations, ε is negligible in all CMIP models (confirming Izumo and Colin 2022 result for CMIP models: using an independent index such as *"h"*=h_{ind_eq+sw} rather than other recharge indices polluted by the tilt mode component leads to a negligible ε; note that we expect oceanic dissipation to be weak, e.g. Fedorov 2010). The correlation skill of the regression is again highly significant: r_h=0.67 [0.67]{0.57}.

CMIP MMM is qualitatively similar to observations, but each model has its own biases. One may hence question how sensitive these results are to ENSO realism in CMIP models. So we have evaluated ENSO in each CMIP model by its ENSO amplitude (STD(T_E)) and spectral shape (namely the ratio between the spectral density in the 1–3 years band and that in 3–15 years band, i.e. STD(1/3-1/1 yr^{-1} band-pass filtered Niño3.4 RSST) divided by STD(1/15-1/3 yr^{-1} band-pass filtered Niño3.4 RSST), close to Bellenger et al. (2014) metrics; more detailed evaluations of CMIP ENSO can be found in earlier references; e.g. Bellenger et al. 2013). We have found some models that are quite far from observations for these two metrics, especially in CMIP5. We have then selected the most realistic CMIP models and have redone Fig. 4 for them (Suppl. Fig. S4). Consistently, the models with the lowest β values (on the left) are rejected, as well as most models with the largest β values. But anyway, the MMM of the RDO parameters are almost similar (to the MMM of all models without selection) for this set of selected models (as well as for CMIP5 and CMIP6 separately). These verifications confirm that the results here are robust, β becoming even more statistically significant when selecting the most realistic models.

The next step is to understand what causes the inter-model diversity in RDO parameters. Knowing that β and F_1 represent distinct physical processes, we expect their strengths to have distinct dependances to the mean state of the climate model. They should depend notably on the SST zonal gradient, the position of the warm pool eastern edge, the mean thermocline depth, themselves possibly related to the typical cold tongue bias, or to the western Pacific precipitation bias (e.g. Bayr et al. 2018, 2019a) with double ITCZ (InterTropical Convergence

549 Zone) bias and related SPCZ (South Pacific Convergence Zone) bias. We can explore this in
550 e.g. CMIP5 models. Fig. 5 shows the inter-model regressions of model mean state (in terms of
551 SST, SLA, precipitation and windstress) onto β and F_1 separately. Note that the patterns related
552 to β and F_1 might seem opposite to each other at first glance but they are actually quite different,
553 not simply opposite in sign. β is as expected larger if the cold tongue is stronger in a model
554 (Fig. 5a), i.e. if the negative mean zonal SST gradient in the western-central equatorial Pacific
555 is stronger (Bayr et al. 2018). The stronger cold tongue there is itself related to larger equatorial
556 easterlies related to larger precipitation over the maritime continent and weaker precipitation
557 in the central Pacific with a horseshoe pattern (Fig. 5e). F_1 strength is more correlated to
558 SLA/thermocline depth mean state (Fig. 5d). A possible explanation is the following: the
559 shallower the mean thermocline is in the southwestern and equatorial Pacific (and also at the
560 southern edge of the north ITCZ, where the North Equatorial Counter Current (NECC) is
561 located), the shallower the STCs lower branches are, the more their transport-weighted
562 temperatures can be affected by thermocline depth anomalies related to a recharged or
563 discharged state. The SLA/thermocline depth mean state changes in Fig. 5d are interestingly
564 related not only to equatorial zonal windstress and equatorial cold tongue, but also to
565 meridionally-asymmetric off-equatorial windstress and related curl (with notably Ekman
566 pumping in the SPCZ forcing off-equatorial Rossby waves propagating westward in the
567 southwest Pacific) associated with mean precipitation (and SST) asymmetric changes (Fig. 5f).
568 To sum up, the strength of the delayed feedback and the effectiveness of the recharge/discharge
569 process vary as a result of the CMIP mean state diversity.
570

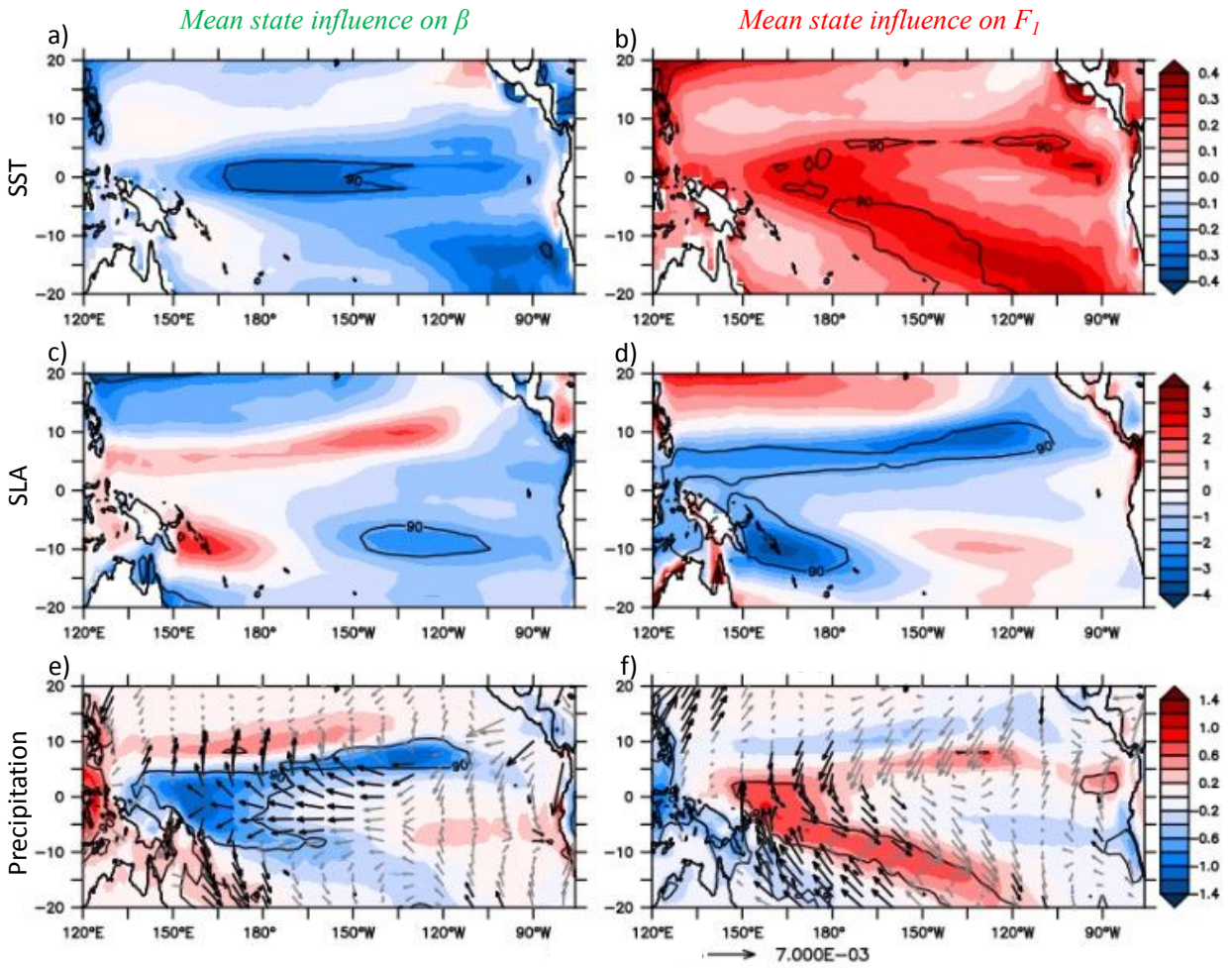

Fig. 5. Mean state influence on β (left) and F_1 (right) in CMIP5 models. Inter-model regressions, onto β and F_1 separately, of model mean state, in terms of SST (upper panels; K), SLA (middle panels, with SLA global mean removed; cm) and precipitation (lower panels; mm day^{-1}; wind stress overlaid in grey, and in black when significant at the 90% level, vectors direction adjusted to panels aspect ratio; N m^{-2}; 90% significant level overlaid as black contours; two-tailed student t-test). Amplitudes per inter-model STD of β or F_1.

For simplicity, we choose the default values $F_1 = 0.12$, $\beta = 0.08$, $R = 0.02$, $F_2 = 0.16$ and $\varepsilon = 0$ month^{-1}, as a simple example to represent their typical values. With these default parameters, the delayed term contribution is two thirds of the recharge term contribution in the temperature tendency equation.

d. RDO eigenvalues and their dependency to parameters

The solutions of the RDO system of differential equations are a vector space, actually of infinite dimension because of the delayed term (see details later on and see also Jin 1997a). To understand the RDO behavior and dependency to parameters, we obtain the eigenvalues by

considering complex solutions of the form $e^{\sigma t}$, with $\sigma = \sigma_r + i\,\sigma_i$, its real part σ_r being the exponential growth or damping rate, and its imaginary part σ_i being the angular frequency. The set of equations (8) and (9) (with ε here neglected for the sake of simplicity; including it is straightforward but makes the below equations heavier; not shown) leads to the following eigenvalues characteristic equation:

$$\sigma^2 - R\sigma + \beta\sigma e^{-\sigma\eta} + F_1F_2 = 0 \qquad (10)$$

This equation in the complex space is equivalent to two real equations:

$$\sigma_r^2 - \sigma_i^2 - R\sigma_r + \beta e^{-(\sigma r\,\eta)}\,(\sigma_r\,cos(\sigma_i\eta) + \sigma_i\,sin(\sigma_i\eta)) + F_1F_2 = 0 \quad \textit{(real part of (10))}$$

$$2\sigma_r\sigma_i - R\sigma_i + \beta e^{-(\sigma r\,\eta)}\,(\sigma_i\,cos(\sigma_i\eta) - \sigma_r\,sin(\sigma_i\eta)) = 0 \quad \textit{(imaginary part of (10))}$$

The solutions can be found numerically as the intersections of the solutions of each of these last two equations in the (σ_r,σ_i) space (Suppl. Fig. S5). The pure DO has an infinity of solutions, while the pure RO has only one. Therefore, the RDO eigenvalues equation (10) has an infinity of solutions and the model has an infinity of eigenmodes. Around the default values of the parameters, the 1st mode is a weakly-damped low-frequency mode (close to observed ENSO main period, and with characteristics relatively close to the RO single mode), with a ~3-yr period and a ~0.02 month^{-1} damping rate (i.e. ~1/4 yr^{-1}). The 2nd mode is a highly-damped higher-frequency mode (~5-month period and ~0.45 month^{-1} damping rate). This 2nd mode can add some high-frequency behavior, making the RDO more appealing than the pure RO which only has one eigenmode close to the 1st RDO mode. Higher eigenmodes are even more damped and of higher frequency.

Eigenvalues equation (10) depends on parameters R, β and on the product F_1F_2, i.e. on the Wyrtki angular frequency $W=(F_1F_2)^{1/2}$, on which the eigenfrequency depends in the RO framework (cf. Lu et al. 2018, Jin et al. 2020). Suppl. Fig. S6def shows the dependency of RDO eigenfrequency $f=\sigma_i/(2\pi)$ to W, β and R separately. Ranges of W, β and R are chosen by considering the observations uncertainties and the inter-model diversity in CMIP data shown in Fig. 4a. For these ranges, the dependency of RDO eigenfrequency to W and β is larger than for the range of R seen in observations and CMIP. Thus, we just focus on the dependency to W and β (Fig. 6b). Both W and β will increase the eigenfrequency similarly. The isofrequency lines can be crudely approximated as diagonal lines with a negative slope close to -1. Actually, if the isofrequency lines were exactly diagonal lines with a negative slope equal to -1 (cf. slope

of the overlayed diagonal line) and monotonically increasing with W and β in that figure 6b, that would mean that f would be proportional to the sum $W+\beta$. I.e. $f \sim f_0 + S\,(W+\beta)$, where f_0 and S would be approximately constant within the CMIP parameter range (with approximately $f_0 \sim 0.008$ month^{-1} and $S \sim 0.09$). The inter-model diversity in RDO eigenfrequency (or also qualitatively in ENSO spectral shape) should hence be approximately proportional to the sum $W+\beta$. Indeed, the ENSO spectral shape in CMIP models is roughly linearly related to $W+\beta$, as evidenced by Fig. 6c, with a high inter-model correlation of 0.75 between $W+\beta$ and ENSO spectral shape among models. The correlation drops to only 0.43 or 0.30 when only W or β alone is used instead of their sum $W+\beta$ (note: correlation with W alone here less good than in Lu et al. (2018) because here W is evaluated from the multi-regression fit for the RDO; in their study the pure RO is considered, so that their recharge term F_{1_RO} will then mix statistically F_1 and β contributions). The sum $W+\beta$ thus explains well the diversity of ENSO frequency among CMIP models. It represents the combined effects of the recharge and delayed feedback processes on ENSO frequency diversity in CMIP models.

The eigen growth rate σ_r has a complex dependence to W and β (Fig. 6a; σ_r dependence to W, β and R separately shown in Suppl. Fig. S6abc). Around CMIP MMM, an increase in W increases σ_r, i.e. decreases the damping, while an increase in β increases the damping. Around W and β default values, σ_r increases quasi-linearly with R (Suppl. Fig. S6c), i.e. with the Bjerknes feedback: $\sigma_r \approx 0.6*(R-0.04)$ (for the RO, we would have $\sigma_r = (R_{RO}-\varepsilon)/2 \approx 0.5*R_{RO}$; Jin et al. 2020). The diversity of these parameters may relate to the diversity in ENSO frequency and ENSO amplitude among models. Interestingly, obs1 as well as about half of CMIP models are near criticality (i.e. almost undamped). If the combination of the three parameters leads to a sufficiently large σ_r so as to become positive, it would lead to an instability. Could this explain some ENSO non-linearities? Or some tipping point effects? Further work would be needed to test this.

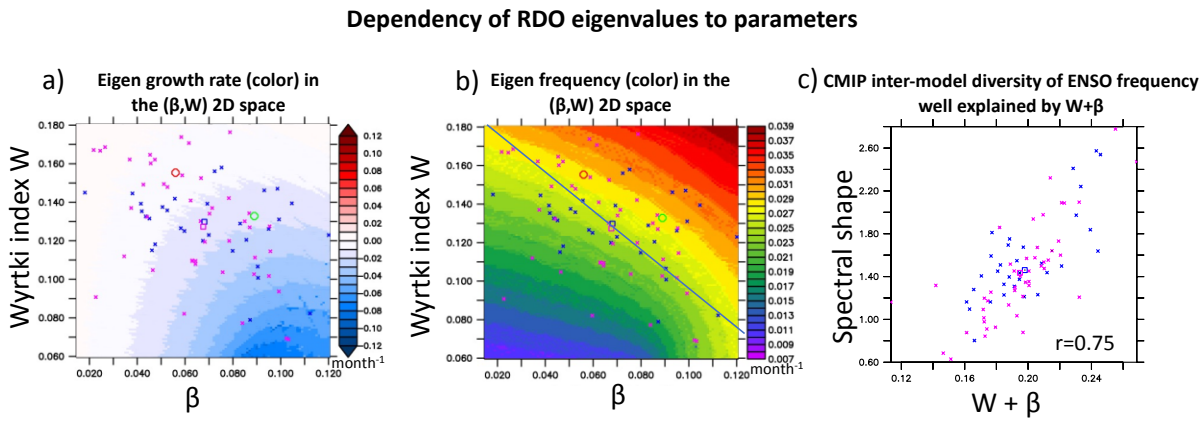

Fig. 6. Dependency of RDO eigenfrequency to parameters. a) RDO eigen growth rate (color shading; month^{-1}) as a function of both β and Wyrtki angular frequency $W=(F_1F_2)^{1/2}$ (W being the eigen angular frequency of the pure RO). **b)** same as a for eigenfrequency (blue diagonal line showing $W= -\beta + constant$). **c)** ENSO spectral shape metric (higher values when ENSO frequency increases, cf. section 2) as a function of the sum $W+\beta$ for each CMIP5 (blue) and CMIP6 (purple) model (with their MMM in squares). In panels a and b, circles show obs1 (red) and obs2 (green).

e. RDO response to stochastic forcing

Now we analyze the RDO response to stochastic forcing. Stochastic forcing is required, as the RDO is damped for the default parameters. To better understand the conceptual model behavior, we have forced the RDO by adding two realistic red noises, one, μ_T, in the right-hand side (rhs) of T_E equation (8) and one, μ_h, in the rhs of h equation (9). The STDs of these red noises ($\sigma_T \approx \sigma_h \approx 0.18$ month^{-1}) are inferred from the two observed residuals of the linear regression fits of equations (8) and (9). These noises are chosen to be independent, as the two observed residuals are only weakly correlated (shared variance < 10%; see also Takahashi et al. 2019 sensitivity tests on this kind of noise choice). Fig. 7a firstly shows an example of the T_E synthetical time series obtained for default parameter values. The system has oscillations, with a frequency modulation, and with low and high-variance decades (similar results over the full 1000-yr period; not shown). The RDO spectral response consistently has a broad peak between ~4 and ~2-yr periods, maximal at ~3-yr (black curve in Fig. 7c), roughly consistent with observed ENSO. Fig. 7b shows the typical evolution of the different terms of the dT_E/dt equation during an ENSO event (i.e. lag-regression onto T_E) for the default synthetic time series shown in Fig. 7a. h (red curve) *l*eads T_E (light blue) by ~10 months, i.e. about a quarter of the ENSO period, as expected because a recharge in h favors a positive T_E (Equation 8), as for usual RO. The delayed feedback effect has a different timing. It is the first to favor the phase reversal, followed by the recharge process. In the RDO, the *negative* noise forcing at lag ~-20 months can already force indirectly the following El Niño onset, notably through the delayed feedback 6 months later. And a *positive* noise (from about -10 months before ENSO peak) can of course also force an El Niño directly.

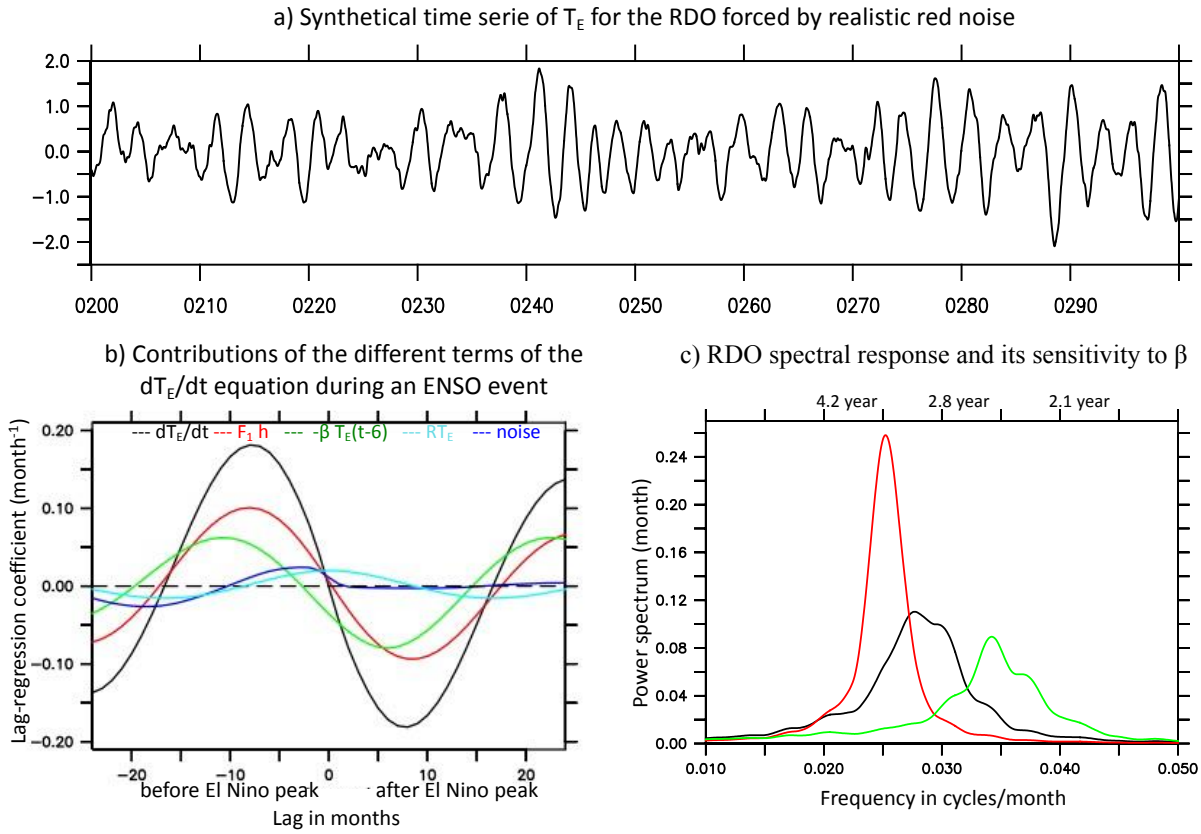

Fig. 7. RDO response to stochastic forcing. a) Synthetical time series of T_E for the linear RDO forced by realistic red noises (added to the rhs of equations 8 and 9; STD(T_E)=0.7 for 1000-yr). **b)** The different terms of the dT_E/dt equation (8) lag-regressed onto T_E, showing their various contributions (unit: month^{-1} per STD of T_E) during the evolution of an ENSO event: dT_E/dt (black), $F_1 h$ (red), $-\beta T_E(t-\eta)$ (green), RT_E (cyan; which also indicates ENSO phase), red noise forcing σ_T (dark blue). The x-axis shows the lag, with negative lags before ENSO peak and positive lags after ENSO peak. **c)** RDO spectral response (i.e frequency response to white noise: power spectrum of T_E for a 1000-yr long white noise forcing) for β default value (0.08 month^{-1}, black), a larger β (0.13 month^{-1}, green; i.e. closer to pure DO with a QuasiBiennal QB mode) and a smaller β (0.05 month^{-1}, red; i.e. close to pure RO with a QuasiQuadriennal QQ mode; for the small β case, the much larger power spectrum is divided by 3 for visualization).

While most contributions are qualitatively similar in obs1 and obs2 (shown in Supp. Fig. S7 for comparison) and are within observations confidence intervals, there are also interesting differences. Observed asymmetries are - by construction - not captured by the simplest RDO framework with only linear terms (cf. sections 5 and 6), e.g. : 1) non-linearities and external forcing included in the residual in equations (8) and (9) are possibly large during ENSO development and mature phase, and damp the reversal to ENSO opposite phase (with the observed 2nd peak of the residual at ~10-month lag not seen for the synthetic time series); 2) the advective-reflective delayed negative feedback seems to play a larger and more systematic role for ENSO events termination and for La Niña onset than for El Niño onset (Suppl. Fig. S7 composites). In summary, within its linear limits, the linear nonseasonal RDO framework

qualitatively matches observations and could help us to better understand the interplay between the recharge and advective-reflective delayed feedbacks in shaping the real-world ENSO.

To illustrate how sensitive the RDO spectral response is to the strength of the advective-reflective delayed negative feedback β, Fig. 7c shows the RDO spectral response for a smaller (0.05) or larger (0.13) β (its default value being 0.08 month^{-1}). In the small β case, the response is of lower frequency (period~3.3-yr) and less damped, with a sharper peak (closer to RO harmonic oscillator behavior). In the large β case, the response is of higher frequency (period~2.5-yr) and highly damped, with a broader spectral range (closer to DO behavior). This broader spectral response can be explained because the DO has a much broader spectral response, thanks to its infinity of eigenmodes, than the RO which has only one eigenfrequency. I.e. the delayed negative feedback brings spectral diversity to the RDO spectrum. To sum up, ENSO spectrum and amplitude are very sensitive to β, i.e. to the advective-reflective delayed negative feedback strength (itself related to the climatological SST zonal gradient).

f. ENSO spatial-temporal diversity in the RDO framework

The RDO model, even in its simplest form, can also explain part of ENSO spatial diversity. To illustrate this, we can exploit the multivariate linear regression based on equation (8.1) for the tendency of temperature $T(x,y,t)$ anywhere in the tropical Pacific. As seen earlier (Fig. 2ab), the $\beta(x,y)$ contribution reminds us of the central Pacific (CP) El Niño spatial pattern, and the $F_1(x,y)$ contribution reminds us of the eastern Pacific (EP) El Niño pattern. Hence, when the RDO is forced by noise, we will have different spatial patterns of $T(x,y,t)$, closer to CP or EP spatial pattern depending on the relative contributions of β and F_1 terms (that notably depend of the frequency of stochastic forcing). The spatial and temporal properties of ENSO are thus strongly dependent on which of the recharge F_1 or delayed β effect is locally dominant. Indeed, we can reconstruct "offline" $T(x,y,t)$ at any location by integrating temporally Equation 8.1 (i.e. the linear combination of $T_E(t)$, $h(t)$ and $T_E(t-6)$), after having obtained synthetic time series of T_E and h from the RDO forced by noise (e.g. time series shown in Fig. 7a). As an example, we have reconstructed $T(x,y,t)$ from the 1000-yr long synthetic time series of T_E and h, using the averages of obs1 and obs2 for the regression coefficients $R(x,y)$, $F_1(x,y)$ and $\beta(x,y)$ (reconstructed $T(x,y,t)$ is high-pass filtered, like long obs2, to remove multidecadal variability that can arise from the time integration, so as to focus on interannual timescales). We can then compare for instance reconstructed Niño4 (CP) and Niño3 (EP) SST variabilities. Niño4 is of significantly higher frequency than Niño3, with an almost-doubled spectral shape metrics: 2.7 for Niño4, 1.5 for Niño3. This is because Niño3 is dominated by $F_1 h$, and h is essentially the

integral of T_E, and thus of lower frequency than T_E. While Niño4 is dominated by $-\beta T_E(t-\eta)$, which has the same spectrum as T_E. The RDO can thus, even in its simplest form, simulates some ENSO spatiotemporal diversity. The RDO captures the fact that part of the CP variability is more biennal (QB) because the delayed feedback is dominant there, and that the EP variability is more quadriennal (QQ; e.g. Wang and Ren 2017) because the slower recharge feedback is dominant there. Note that additionally, there is in observations a decadal component of CP ENSO (Behera and Yamagata 2011, Sullivan et al. 2016, Capotondi et al. 2020) that could be implemented in the RDO framework, e.g. through a decadal modulation of the mean state (e.g. Zhang et al. 2019) modulating RDO parameters (possibly through STCs; Zeller et al. 2019, 2021).

5. Non-linear seasonal RDO

The simplest RDO framework, linear and non-seasonal, can be obviously improved by adding: 1) the seasonal cycles of RDO parameters, 2) asymmetries/non-linearities, e.g. quadratic terms and a multiplicative noise. We have added them separately, and then all together in the most comprehensive RDO version, the non-linear seasonal RDO. We have also tested the influence of each non-linear parameter on the phase diagram trajectories (Supplementary Materials). The take-home message is that, with seasonal cycle, non-linearities and multiplicative noise added, the RDO is even more realistic, and still has robust and highly-significant F_1 and β coefficients, i.e. the non-linear seasonal RDO is more realistic than the non-linear seasonal RO or DO.

a. Seasonality of RDO parameters

Knowing the ENSO observed seasonal phase-locking, the first improvement to do to the RDO is to allow all its parameters to vary seasonally. The simplest seasonality we can add for parameters is, for instance for β parameter, of the form $\beta = \beta_0 + \beta_{seas}\, sin(\omega t-\lambda) = \beta_0 + \beta_S\, sin(\omega t) + \beta_C\, cos(\omega t)$. $\beta = \beta_0 + \beta_{seas}\, sin(\omega t-\lambda)$ looks mathematically 'nicer', by having amplitude β_{seas} and phase λ separately, than $\beta = \beta_0 + \beta_S\, sin(\omega t) + \beta_C\, cos(\omega t)$. Yet the later form is more convenient, notably to compute intervals of confidence and when we want to compare different observations and/or models, as the phase λ is modulo(2π) and we for instance cannot compute a multi-model mean (MMM) of λ directly from the λ of each model (it would only be possible

by first computing the β_S and β_C MMM, to then convert them into β_{seas} and λ values). And β_S and β_C are straightforward to interpret: here $t=0$ on January 1st, so that $sin(\omega t)$ is maximum on April 1st and minimum on October 1st, and cos(ωt) is maximum on January 1st and minimum on July 1st. As the number of parameters to fit is now multiplied by 3, i.e. 9 for T_E tendency equation and 6 for h one, we essentially focus on the results based on our longest reanalysis data, 'hist', and on CMIP historical runs, for which the number of effective degrees of freedom is sufficiently large (obs2 still shown in Suppl. Fig. S8; note however the larger uncertainty bars when estimating RDO seasonally-varying parameters with obs2; obs1 is not shown, being obviously too short). In a nutshell, the correlation skills r_T and r_h of dT_E/dt and dh/dt equations strongly increase by including the seasonal cycle (compare panel c to panel b in Suppl. Fig. S8). And the RDO still has a robust and highly-significant β coefficient for the delayed feedback (with β_0 even two times larger than $F_{1,0}$ in hist; Suppl. Fig. S8c).

Let us now describe each parameter's seasonal cycle (Fig. 8abc shown here for the non-linear version of the seasonal RDO, which has a similar seasonality to its linear version; cf. comparison of each parameter's seasonal coefficients in Suppl. Fig. S8). We here focus on hist-based parameters, as this should be our most realistic estimates, keeping in mind the limit of historical oceanic reanalyses, the actual "truth" being possibly between hist, shorter obs2, and CMIP estimates. To interpret the coefficients seasonality, keep in mind that their actual contribution to T_E and h tendencies will be the product of the coefficient and of its associated term. E.g. F_2T_E actual contribution to dh/dt will be larger in boreal winter than F_2 alone, when T_E interannual STD peaks. Let us start with R. R has a strong seasonal cycle, with $-R_S \sim R_0 > 0$. R is the largest around September and the lowest in March, favoring a peak of ENSO around December, as expected from previous studies (e.g. Jin et al. 2020). F_1 has a relatively-weak seasonal cycle, being slightly larger around January-March and weaker around July-September, likely because the climatological equatorial upwelling in the central-eastern Pacific (170ºW-120ºW) is the strongest in January-March and the weakest in July-September. β_0 is highly significant (even above 99% level) and larger than $F_{1,0}$ in hist (but not in obs2 and CMIP). β has a large seasonal cycle, dominated by β_S, i.e. is maximal in spring, possibly because of the seasonal cycle in the product $C\mu_C$ between the coupling parameter μ_C and the climatological zonal SST gradient C (cf. section 3.2), and/or because of Indian Ocean Dipole (IOD, an equivalent of El Niño for the Indian Ocean, e.g. Saji et al. 1999) delayed influence (Izumo et al. 2010) likely partly included in the delayed term. The difference between F_1 and β seasonal cycles further confirms that F_1 and β terms represent distinct physical processes.

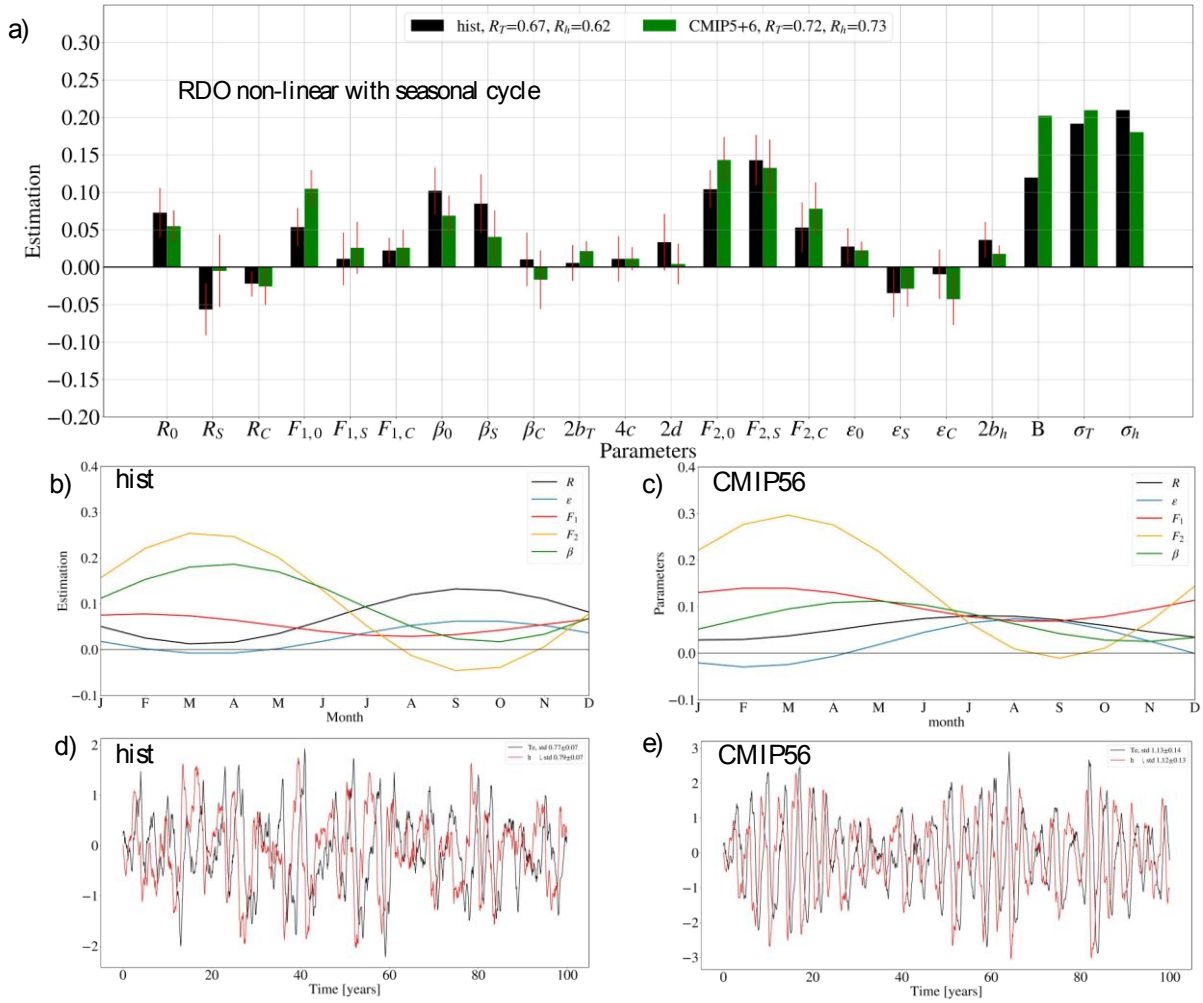

Fig. 8. The non-linear seasonal RDO. a) bar plot showing each parameter of equations 11 and 12, estimated by a multivariate fit (with B and σ_T estimated as in An et al. 2020). To represent the actual contribution of the non-linear terms for strong ENSO events, their parameters are multiplied by 2 for quadratic terms and by 4 for the cubic term, for a fair comparison with linear parameters such as R, F_1 and β (as for a strong 2STD event, we will have e.g. $F_1T_E = 2F_1$, $b_TT_E^2 = 2*2b_T$, $cT_E^3 = 2*4c$). The correlation skills r_T and r_h are given above the bar plot. For hist (black), the red line shows the 95% interval of confidence. For CMIP MMM (green), it represents the ±1 inter-model STD (among all CMIP). **b)** seasonal cycles of the main RDO parameters estimated from the fit on hist. **c)** same as b but for CMIP MMM. **d)** 100-yr long timeseries of hist-based nonlinear seasonal RDO (STD given for the average of fifty 100-yr long timeseries). **e)** as d, but for CMIP-based RDO.

For *dh/dt* equation (1), which is the same for the RO and RDO, previous studies (e.g. Chen and Jin 2020) of the RO had usually considered F_2 to be seasonally-constant, supposing that its seasonal cycle was negligible. Actually, F_2 has a large significant and robust seasonality in all our estimates (Fig. 8abc and Suppl. Fig. S8). This is the first study to our knowledge that shows this F_2 seasonality for the RO/RDO recharge equation. F_2 represents the efficiency of

the recharge for a given T_E anomaly (e.g. 1K). $F_{2,S}$ is as large as the constant component $F_{2,0}$ in hist. F_2 is maximum in early spring (Feb.-Apr.) and negligible in early autumn (Aug.-Oct.), with of course differences among observations and CMIP estimates. ε_0 is weakly positive, ~0.02 month^{-1}, with some seasonal cycle, maximum in hist ($\varepsilon_S < 0$) in fall and negligible in spring. Taking into account all these seasonal cycles lead to a more realistic RDO behavior with seasonal phase-locking and richer combination tones (e.g. Stuecker et al. 2013), especially when including non-linearities, i.e. the full non-linear seasonal RDO version described hereafter.

b. Adding non-linearity: the non-linear seasonal RDO

Above we had neglected asymmetries/non-linearities for the sake of simplicity. The next step is to include such terms. We can add to the dT_E/dt equation (8) the quadratic and cubic terms $+b_T T_E^2 - c\ T_E^3 + d\ T_E\ h$. They notably represent the non-linear response of convection (and of related windstress) to T_E (e.g. Choi et al. 2013; Takahashi et al. 2019; Jin et al. 2020; An et al. 2020; Dommenget and Al Ansari 2022; Srinivas et al. 2022, 2024). We can also add a multiplicative noise (e.g. Jin et al. 2007; Graham et al. 2015, their equation 23). We can add to the dh/dt equation (9) a quadratic term $-b_h T_E^2$. I.e. the discharge during an El Niño of amplitude T_{E_0} is larger than the recharge during a La Niña of similar amplitude $-T_{E\_0}$, notably because equatorial zonal windstress anomalies are of larger amplitude and fetch (Srinivas et al. 2024) and are further to the east (e.g. Izumo et al. 2019; note that we could add even further complexity, e.g. a non-linearity of the delayed term, as in DiNezio and Deser 2014, and a state-dependency of F_2 as in Iwakiri and Watanabe 2022 to even better simulate long-lasting La Niña). Thus, the non-linear seasonal RDO equations are:

$$dT_E/dt = R\ T_E + F_1\ h - \beta\ T_E(t-\eta) + b_T T_E^2 - c\ T_E^3 + d\ T_E\ h + \mu_T(1+BT_E) \qquad (11)$$

$$dh/dt = -F_2\ T_E - \varepsilon\ h\ - b_h T_E^2 + \mu_h \qquad (12)$$

Where μ_T and μ_h are red noises with standard deviations σ_T and σ_h respectively, and with a 5-day decorrelation time (cf. section 2). B represents the strength of the multiplicative noise (i.e. larger noise during El Niño than during La Niña). Here we have tried to keep the notations as much as possible consistent with the (soon open-source) Community RO model under development presently, to which we participate (Vialard et al. 2023, personal communication; see also review of An et al. 2020).

847 Now we have 12 parameters to fit for equation (11) (as we assume no seasonality of the
848 non-linear terms, and as B and σ_T are separately estimated from the residual distribution), and
849 7 parameters for equation (12), shown in Fig. 8a and Suppl. Fig. S8. The first result is that the
850 RDO is still robust and better than the RO, when including non-linearity and multiplicative
851 noise in addition to seasonality. β_0 is large and significant (even at the 99% level in hist and
852 CMIP). Including this delayed effect to the RO clearly increases the skill and explained
853 variance of dT_E/dt equation (in hist: correlation skill r_T =0.60 to 0.67, i.e. a relative increase of
854 explained variance by 25%, r_T^2 increasing from 36% to 45%; in CMIP: r_T =0.67 to 0.72, i.e.
855 increase of explained variance by 16%, r_T^2 increasing from 45% to 52%). The results for CMIP
856 and hist are qualitatively consistent, but quantitatively different. The largest differences are for
857 F_1 and β relative contributions, β being larger than F_1 in hist (vice versa for CMIP), as
858 aforementioned. The nonlinearities d and b_h are stronger in hist. Fig. 8de shows the generated
859 synthetic time series of T_E, for hist and CMIP-MMM parameters respectively. They are quite
860 different too. The synthetic time series for hist look more realistic (asymmetry, irregularity).
861 Most CMIP models have a bias in ENSO nonlinearity/asymmetry (Hayashi et al. 2020); thus,
862 that their RDO also fails to reproduce asymmetry is expected. The larger irregularity of hist-
863 based RDO could be partly explain by the larger β/F_1 ratio in hist than in CMIP. Fig. 9b shows
864 the trajectories in the (T_E,h) phase space of the hist-based nonlinear seasonal RDO. They are
865 qualitatively similar to hist ones (Fig. 9a), with similar asymmetries, namely larger extreme El
866 Niño events with larger and faster discharges than extreme La Niña (see e.g. Iwakiri and
867 Watanabe 2022 for processes driving long-lasting La Niña).
868

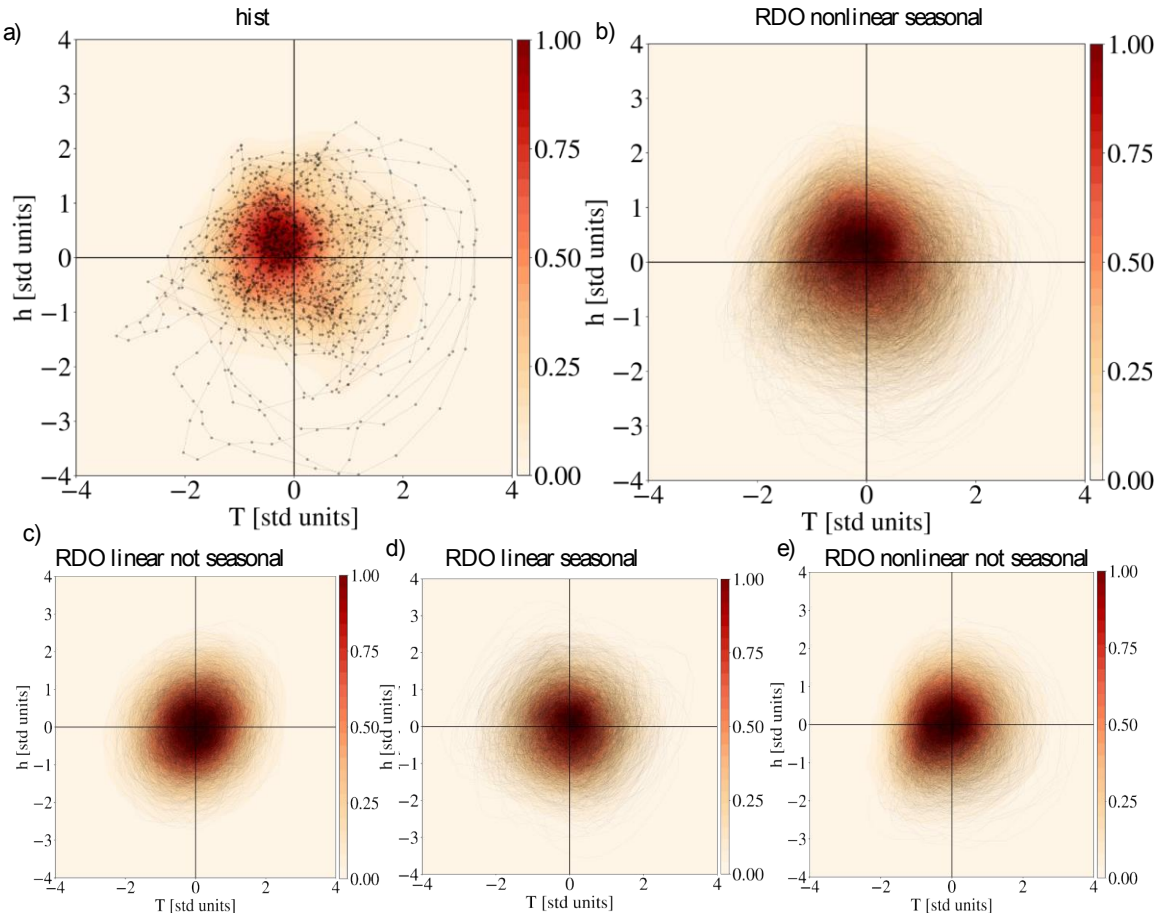

869

870 **Fig. 9. a) Phase diagram *(T_E,h)*** of hist observations/reanalysis. The trajectories are shown in thin grey
871 curves, and their probability density function (PDF) in color shading. **b)** phase diagram *($T_{E\_synthetic}$,$h_{\_synthetic}$)*
872 of 50 100-yr long synthetical time series obtained by forcing hist-based non-linear seasonal RDO by red
873 noises. **c)** as b but for the hist-based simplest linear RDO without seasonality (and without multiplicative
874 noise, i.e. B=0). **d)** as c but adding seasonality. **e)** as c but adding non-linearities (including multiplicative
875 noise). Note that, when the distribution is shifted with extreme El Niño and discharge being stronger, the
876 PDF maximum, i.e. the most likely points, is shifted towards slightly negative T_E and positive *h* anomalies
877 (mean removed).

878

879 To highlight visually the role of each non-linear term in the non-linear seasonal RDO (for
880 the set of parameters obtained from hist), Suppl. Fig. S9 shows RDO phase diagram when each
881 of them is artificially removed. E.g. the absence of $b_h T_E^2$ in S9b leads to less extreme discharge
882 (there is still some asymmetry in the recharge/discharge due to the non-linear terms in the
883 dT_E/dt equation, but weaker than with b_h included). I.e. S9b shows that $b_h T_E^2$ role makes the
884 discharge more extreme during strong El Niño. Multiplicative noise associated to B sustains
885 strong El Niño (i.e. the lower-right quarter of the phase diagram; Suppl. Fig. S9d). The role of
886 $b_T T_E^2$ should be to increase El Niño and reduce La Niña. However, in the hist case shown here

where b_T is weak, this effect is hard to see in Suppl. Fig. S9e (it would be more seen in CMIP-based RDO case). The cubic term $-cT_E^3$ reduces very extreme T_E events (for both El Niño and La Niña events; Suppl. Fig. S9f). The $d\,T_E\,h$ favors larger « La Niña+discharged state » events in the lower-left quadrant and diminishes them in the upper-right quadrant, 'tilting' the phase diagram. Note that this detailed analysis of the role of each non-linear term remains qualitatively valid for the RO framework.

6. Conclusion

a. Summary

We have developed a hybrid recharge-delayed oscillator, the RDO, more realistic than the stand-alone RO or DO (schematics in Fig. 1). This RDO can help us to improve our theoretical understanding of ENSO and of its irregularity, diversity and complexity. We have shown that the ENSO temperature tendency dT_E/dt results essentially from the combination of two distinct negative feedback mechanisms with distinct spatial distributions, in addition to the Bjerknes positive feedback:

(1) the slow long-term recharge during La Niña (discharge during El Niño) with a timescale of ~1-2 years. This slow recharge process takes place over the equatorial and southwestern Pacific independently of the fast tilt mode, i.e. $\textit{"h"} = h_{ind\_eq+sw}$. This long-term recharge firstly affects the oceanic mixed layer temperature tendency in the central-eastern equatorial Pacific by favoring advection of warmer subsurface waters by the climatological STCs/TCs and EUC towards the equatorial upwelling, i.e. $-U_{clim}\,\partial T'/\partial x$ and $-W_{clim}\,\partial T'/\partial z$.

(2) the advective-reflective delayed negative feedback of ~6 months. This delayed feedback firstly affects the oceanic mixed layer temperature tendency in the western-central equatorial Pacific by anomalous upper layer zonal current advecting the climatological temperature zonal gradient through wave processes, i.e. $-U'\,\partial T_{clim}/\partial x$.

These two *distinct* processes are both essential for equatorial Pacific SST variability and so for the coupled system. Hence, rather than stating that the recharge oscillator (RO) and delayed oscillator (DO) are two different formal ways of representing the same physical process as done usually in previous studies, the present results based on observations and 79 CMIP models show that these two different physical processes with different timescales should be distinguished in the equations. They can be formally incorporated in the RDO. This hybrid oscillator has qualitatively-realistic spectral characteristics (with a wider spectral peak than the

RO) and lead-lag relationships. The inclusion of the delayed term $-\beta T_E(t-\eta)$ [with η = 6 months] favors a more irregular, and possibly chaotic, behavior when forced by stochastic forcing. RDO eigenvalues are highly sensitive to both the Wyrtki angular frequency $W=(F_1F_2)^{1/2}$ and the β parameter (representing respectively the strengths of the RO and DO components), themselves sensitive to the mean state (and thus to CMIP model biases). We have notably shown that the main RDO eigenfrequency is approximately linearly related to the sum $W+\beta$. I.e. ENSO frequency increases not only if W is larger, but also if the advective-reflective delayed feedback is larger. Furthermore, by taking into account that the advective-reflective delayed feedback (respectively recharge feedback) is larger in the western-central Pacific (respectively eastern equatorial Pacific), each feedback having its own time scale, we can reconstruct equatorial SST at any longitude within the RDO framework, and simulate some ENSO spatiotemporal diversity.

Finally, we have shown that the simple RDO framework is robust and more realistic than the RO framework, and could be significantly improved by adding: 1) the seasonal cycles of RDO parameters, 2) asymmetries/non-linearities, e.g. quadratic/cubic terms and a multiplicative noise. These non-linearities added to seasonality further increase the system's complexity and possibly make it more irregular and chaotic, and thus increase potentially ENSO spatiotemporal diversity. We have also investigated the influence of each non-linear term on the (T_E,h) phase space trajectories, an investigation that is also useful for the RO framework.

b. Discussion on possible improvements of the RDO

This latest and more refined RDO version could still be further improved by adding: 1) influences external to the tropical Pacific, 2) a third box in the model to explicitly allow for more spatial diversity of ENSO events.

External influences to add are notably the two-way interaction of the IOD with ENSO (e.g. Izumo et al. 2010, Luo et al. 2010, Jourdain et al. 2016), the mean tropical Indian and Atlantic Oceans warming/cooling, which act as negative feedbacks to ENSO (e.g. Dommenget and Yu 2017), and the north and south tropical Pacific (e.g. Alexander et al. 2010). E.g. the IOD can also force the advective-reflective delayed feedback: a negative IOD forces easterly anomalies in the western Pacific, thereby favoring positive zonal current anomalies ~6 months later in the western-central equatorial Pacific. Hence a perspective would be to add a third variable in the system, the IOD as a forcing external to the tropical Pacific coupled to ENSO (mathematically

like in Kug and Kang 2006 and Frauen and Dommenget 2012, but for the IOD rather than for the Indian Ocean basin-wide SST).

Here our original aim was not to capture the various ENSO flavors, i.e. the ENSO diversity continuum from extreme EP El Niño to CP El Niño Modoki events, that have partly distinct global teleconnections. For the sake of simplicity, we have focused on ENSO events defined with the usual Niño3.4 region. Still, the RDO framework has allowed us to reconstruct ENSO spatiotemporal diversity, at least partly, even without adding non-linear terms (Fig. 2ab). While in the RO framework, nonlinearities are needed to capture ENSO diversity (Thual and Dewitte 2023). Adding seasonality and nonlinearities to the RDO (section 5) can increase simulated ENSO diversity/complexity even more. The next step is to implement our RDO approach in a three-box conceptual model (i.e. west, central and east Pacific boxes), such as in Fang and Mu (2018), Geng et al. (2020) and Chen et al. (2022) but with a physically-based formalization of the equations inspired by the above RDO approach.

c. Implications and perspectives

The RO still remains useful, being the simplest ENSO conceptual model. We still appreciate its use. But it implicitly mixes two physically different processes, the zonal advective and thermocline feedbacks. The RDO does not. It is more physical and captures the spatial and frequential diversity of ENSO, while still remaining simple enough.

The RDO set of equations may formally look partly like a simplification of the unified oscillator of Wang (2001), which was shown by Graham et al. (2015) to be less realistic than the simple DO. However, here the RDO set of equations is for (T_E, h_{ind_eq+sw}) orthogonal space instead of (T_E, h_{eq}) non-orthogonal space. And the various terms of the RDO equations represent clear distinct physical mechanisms, conversely to the unified oscillator as pointed out by Graham et al. (2015).

For ENSO operational forecast diagnostics, Izumo and Colin (2022) have shown that the pair of coordinates (T_E, h_{ind_eq+sw}) is more relevant to describe the RO system trajectory than the usual pairs (T_E, h_{eq}) or (T_E, h_w). Here the RDO realism furthermore suggests that an additional useful term to take into account to operationally diagnose the system state is $T_E(t-\eta)$ as an indicator of the advective-reflective delayed negative feedback effect, e.g. when diagnosing the present oceanic state or for operational forecasts. The RDO framework should also be useful to study ENSO predictability with information theory (Fang and Chen 2023).

Background interdecadal changes in the sum $W+\beta$ may favor the Quasi-Quadriennal (QQ) or Quasi-Biennal (QB) ENSO regimes (e.g. Jin et al. 2020), and might have a role in ENSO

984 'regime shifts' and ENSO diversity. The QQ regime is more associated with large EP El Niño
985 events, for which the thermocline feedback (W) plays a central role. While the QB regime is
986 more associated with moderate CP El Niño events more driven by the zonal advection feedback
987 (β). The RDO framework (possibly adding a third box as suggested above) could help us in
988 understanding the differences between the decades with weak and strong ENSO variances and
989 with differences in ENSO frequency and flavors, possibly related to decadal mean state
990 changes influencing β and W relative strengths (Chen et al. 2022, Chen and Fang 2023), as well
991 as the ENSO response to climate change (e.g. Cai et al. 2021; Shin et al. 2022).
992 There are several pathways to better understand theoretically the RDO model. How
993 combining the RO and DO influences the chaotic behavior of the delayed differential equation
994 system (e.g. Tziperman et al. 1995, Keane et al. 2016), as for the case of two coupled oscillators
995 interacting with noise. A mathematical approach with series as in Power (2011) for the DO
996 could be developed for the RDO. For the nonlinear seasonal RDO, an approach based on a
997 Fokker-Planck equation could help (An et al. 2021). Then we could use an intermediate
998 approach similar to Yu et al. (2015),who combined the RDO to a slab ocean coupled to an
999 AGCM to capture ENSO dynamics and diversity. But we could modify their intermediate
1000 model by (1) using an independent recharge index such as h_{ind_eq+sw}, (2) adding the delayed
1001 negative feedback with its shorter timescale.

1002 The RDO could help us to reconcile ENSO theories. It would be very interesting to redo
1003 detailed analyses testing each ENSO oscillator, such as Graham et al. (2015) approach, and/or
1004 Linz et al. (2014) approach based on transfer functions, in light of the present results, and see
1005 whether theories, climate models and observations would better agree if one keeps RO and DO
1006 processes distinguished through the hybrid RDO framework developed here. To conclude,
1007 using this simple RDO framework could help us to improve ENSO theories, climate model
1008 diagnostics and forecasts.
1009

1010 *Acknowledgments.*

1011 First we would like to thank the three reviewers for their highly-relevant reviews. They
1012 have pushed us to demonstrate even further the RDO framework potential, and that have also
1013 clearly improved the readability of the manuscript. T.I. would like to thank his excellent former
1014 student, Timothée Jullien de Pommerol, for downloading the CMIP6 data, and for
1015 implementing a first Python version of the nonlinear seasonal RO, that B.P. has then further
1016 improved, as well as Jérôme Vialard and Matthieu Lengaigne for interesting discussions at a

much earlier stage of this work. M.C. would like to thank Steven Sherwood for his essential support, supervision, and mentoring, in particular throughout the pandemic, which made this collaboration possible. We also would like to thank Soong-Ki Kim, Sen Zhao and Jérôme Vialard for interactions and discussions on the non-linear seasonal RO implemented by B.P. in Python in the Community RO Model framework initiated by Jérôme Vialard (who we really thank for this excellent initiative). T.I. and M.C. would like to thank UPF team for their continuing support, as well as for hosting M.C. because of COVID-related closed Australian borders; this latter fact was paradoxically essential for allowing us to make this work mature. T.I. and B.P. are funded mainly by IRD core budget, with some funding from UMR241 SECOPOL (ex-EIO) laboratory and ANR ARISE project.

Data Availability Statement.

All data used is open data: OISSTv2 (https://psl.noaa.gov/data/gridded/data.noaa.oisst.v2.html), ERA5 and ORAS5 (https://www.ecmwf.int), Copernicus SLA (https://doi.org/10.48670/moi-00148), SODA (https://www2.atmos.umd.edu/~ocean/), Tropflux (https://incois.gov.in/tropflux/), HadiSSTv1.1 (https://www.metoffice.gov.uk/hadobs/hadisst/), CMIP models (https://wcrp-cmip.org), GPCP (https://psl.noaa.gov/data/gridded/data.gpcp.html), 20CR (https://psl.noaa.gov/data/20thC_Rean/). We acknowledge use of NOAA pyferret open source software for analyses and figures, as well as python.

1037 APPENDIX

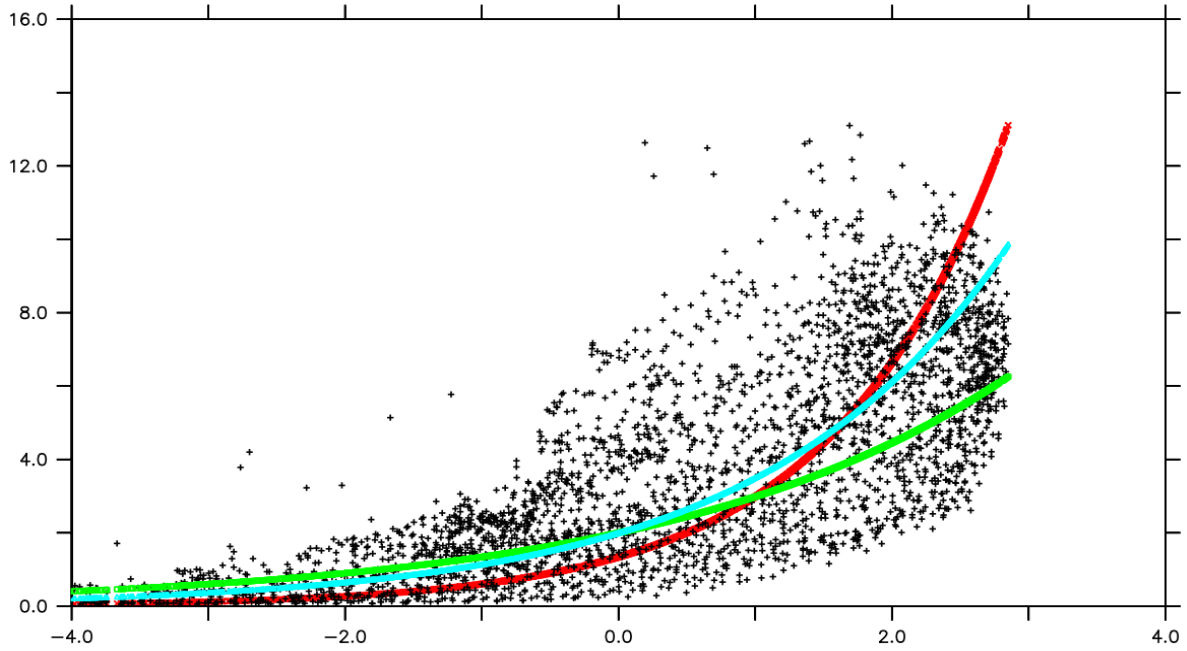

1038
1039
1040 **Fig. A1. Verification of the approximated formula for the sensitivity of precipitation to RSST.**
1041 Scatterplot of $Precip_{clim}$ (monthly GPCP precipitation, mm/day) to $RSST_{clim}$ (monthly OISST, regridded on
1042 GPCP grid; K) in the equatorial Pacific (5ºN-5ºS, 120ºE-80ºW). The default fit in blue is $P(RSST) = 2\ e^{0.56RSST}$, the factor 0.56 inspired by Tippett et al. cyclogenesis index. Tests using other exponential forms,
1044 e.g. $P(RSST) = 2\ e^{0.4RSST}$ (green) or $P(RSST) = 2\ e^{0.8(RSST-0.5)}$ (red) show that the default approximation is
1045 qualitatively reasonable. Fig. 2cd redone with these other forms lead to qualitatively-similar results, with
1046 delayed term contribution increasing if the factor in the exponential increases, as it gives more weight to
1047 regions with higher climatological RSST (vice versa if it decreases).

1048 REFERENCES

1049 Adler, R.F., G.J. Huffman, A. Chang, R. Ferraro, P. Xie, J. Janowiak, B. Rudolf, U. Schneider,
1050 S. Curtis, D. Bolvin, A. Gruber, J. Susskind, and P. Arkin, 2003: The Version 2 Global
1051 Precipitation Climatology Project (GPCP) Monthly Precipitation Analysis (1979-
1052 Present). J. Hydrometeor., 4,1147-1167.

1053 Alexander, M. A., Vimont, D. J., Chang, P., & Scott, J. D. (2010). The impact of extratropical
1054 atmospheric variability on ENSO: Testing the seasonal footprinting mechanism using
1055 coupled model experiments. *Journal of Climate*, *23*(11), 2885-2901.

1056 An, S. I., Tziperman, E., Okumura, Y. M., & Li, T. (2020). ENSO irregularity and
1057 asymmetry. *El Niño Southern Oscillation in a changing climate*, 153-172.

1058 An, S. I., Kim, S. K., & Timmermann, A. (2020). Fokker–Planck dynamics of the El Niño-
1059 Southern Oscillation. *Scientific reports*, *10*(1), 16282.

1060 Ashok, K., Behera, S. K., Rao, S. A., Weng, H., & Yamagata, T. (2007). El Niño Modoki and
1061 its possible teleconnection. *Journal of Geophysical Research: Oceans*, *112*(C11).

1062 Ballester, J., Bordoni, S., Petrova, D., & Rodó, X. (2015). On the dynamical mechanisms
1063 explaining the western Pacific subsurface temperature buildup leading to ENSO
1064 events. *Geophysical Research Letters*, *42*(8), 2961-2967.

1065 Ballester, J., Bordoni, S., Petrova, D., & Rodó, X. (2016). Heat advection processes leading to
1066 El Niño events as depicted by an ensemble of ocean assimilation products. *Journal of*
1067 *Geophysical Research: Oceans*, *121*(6), 3710-3729.

1068 Barnston, A. G., Tippett, M. K., L'Heureux, M. L., Li, S., & DeWitt, D. G. (2012). Skill of
1069 real-time seasonal ENSO model predictions during 2002–11: Is our capability
1070 increasing?. *Bulletin of the American Meteorological Society*, *93*(5), 631-651.

1071 Barnston, A. G., Tippett, M. K., Ranganathan, M., & L'Heureux, M. L. (2019). Deterministic
1072 skill of ENSO predictions from the North American Multimodel Ensemble. *Climate*
1073 *Dynamics*, *53*(12), 7215-7234.

1074 Battisti, D. S., & Hirst, A. C. (1989). Interannual variability in a tropical atmosphere–ocean
1075 model: Influence of the basic state, ocean geometry and nonlinearity. *Journal of*
1076 *Atmospheric Sciences*, *46*(12), 1687-1712.

1077 Bayr, T., Latif, M., Dommenget, D., Wengel, C., Harlaß, J., & Park, W. (2018). Mean-state
1078 dependence of ENSO atmospheric feedbacks in climate models. *Climate*
1079 *Dynamics*, *50*(9), 3171-3194.

1080 Bayr, T., Wengel, C., Latif, M., Dommenget, D., Lübbecke, J., & Park, W. (2019a). Error
1081 compensation of ENSO atmospheric feedbacks in climate models and its influence on
1082 simulated ENSO dynamics. *Climate dynamics*, *53*(1), 155-172.
1083 Behera S, Yamagata T. Imprint of the El Niño Modoki on decadal sea level changes.
1084 Geophysical Research Letters. 2010 Dec;37(23).
1085 Bellenger, H., Guilyardi, É., Leloup, J., Lengaigne, M., & Vialard, J. (2014). ENSO
1086 representation in climate models: From CMIP3 to CMIP5. *Climate Dynamics*, *42*(7),
1087 1999-2018.
1088 Blanke B, Raynaud S. Kinematics of the Pacific equatorial undercurrent: An Eulerian and
1089 Lagrangian approach from GCM results. Journal of Physical Oceanography. 1997 Jun
1090 1;27(6):1038-53.
1091 Bosc, C., & Delcroix, T. (2008). Observed equatorial Rossby waves and ENSO- related warm
1092 water volume changes in the equatorial Pacific Ocean. *Journal of Geophysical Research:*
1093 *Oceans*, *113*(C6).
1094 Boulanger, J. P., & Menkes, C. (2001). The Trident Pacific model. Part 2: role of long
1095 equatorial wave reflection on sea surface temperature anomalies during the 1993–1998
1096 TOPEX/POSEIDON period. *Climate Dynamics*, *17*(2), 175-186.
1097 Boulanger, J. P., Menkès, C., & Lengaigne, M. (2004). Role of high-and low-frequency winds
1098 and wave reflection in the onset, growth and termination of the 1997–1998 El
1099 Niño. *Climate dynamics*, *22*(2-3), 267-280.
1100 Bretherton, C. S., Widmann, M., Dymnikov, V. P., Wallace, J. M., & Bladé, I. (1999). The
1101 effective number of spatial degrees of freedom of a time-varying field. *Journal of*
1102 *climate*, *12*(7), 1990-2009.
1103 Bunge, L., & Clarke, A. J. (2009). A verified estimation of the El Niño index Niño-3.4 since
1104 1877. *Journal of Climate*, *22*(14), 3979-3992.
1105 Burgers, G., F.-F. Jin, and G. J. van Oldenborgh (2005), The simplest ENSO recharge
1106 oscillator, Geophys. Res. Lett., 32, L13706, doi:10.1029/2005GL022951.
1107 Cai, W., Santoso, A., Collins, M., Dewitte, B., Karamperidou, C., Kug, J. S., ... & Zhong, W.
1108 (2021). Changing El Niño–Southern oscillation in a warming climate. *Nature Reviews*
1109 *Earth & Environment*, *2*(9), 628-644.
1110 Capotondi, A. (2013). ENSO Diversity in the NCAR CCSM4 Climate Model. J. Geophys. Res.
1111 Oceans 118, 4755–4770. doi:10.1002/jgrc.20335

1112 Capotondi, A., Wittenberg, A. T., Newman, M., Di Lorenzo, E., Yu, J. Y., Braconnot, P., ... &
1113 Yeh, S. W. (2015). Understanding ENSO diversity. *Bulletin of the American*
1114 *Meteorological Society*, *96*(6), 921-938.
1115 Chen, N., Fang, X., & Yu, J. Y. (2022). A multiscale model for El Niño complexity. *npj*
1116 *Climate and Atmospheric Science*, *5*(1), 16.
1117 Chen, N., & Fang, X. (2023). A simple multiscale intermediate coupled stochastic model for El
1118 Niño diversity and complexity. Journal of Advances in Modeling Earth Systems, 15(4),
1119 e2022MS003469.
1120 Chen HC, Jin FF. Fundamental behavior of ENSO phase locking. Journal of Climate. 2020
1121 Mar 1;33(5):1953-68.
1122 Choi, K.-Y., Vecchi, G. A., & Wittenberg, A. T. (2013). ENSO transition, duration, and
1123 amplitude asymmetries: Role of the nonlinear wind stress coupling in a conceptual
1124 model. *Journal of Climate, 26*(23), 9462–9476. https://doi.org/10.1175/JCLI-D-13-
1125 00045.1
1126 Clarke, A. J. (1994). Why are surface equatorial ENSO winds anomalously westerly under
1127 anomalous large-scale convection?. *Journal of climate*, *7*(10), 1623-1627.
1128 Clarke, A. J., Van Gorder, S., & Colantuono, G. (2007). Wind stress curl and ENSO
1129 discharge/recharge in the equatorial Pacific. *Journal of Physical Oceanography*, *37*(4),
1130 1077-1091.
1131 Clarke, A. J. (2008). *An introduction to the dynamics of El Niño and the Southern Oscillation*.
1132 Elsevier.
1133 Clarke, A. J. (2010). Analytical theory for the quasi-steady and low-frequency equatorial ocean
1134 response to wind forcing: The “tilt” and “warm water volume” modes. *Journal of*
1135 *physical oceanography*, *40*(1), 121-137.
1136 Crespo, L. R., M. Belén Rodríguez-Fonseca, I. Polo, N. Keenlyside, and D. Dommenget, 2022:
1137 Multidecadal variability of ENSO in a recharge oscillator framework. Environ. Res.
1138 Lett., 17, 074008, https://doi.org/10.1088/1748-9326/ac72a3.
1139 DiNezio PN, Deser C. Nonlinear controls on the persistence of La Niña. Journal of Climate.
1140 2014 Oct 1;27(19):7335-55.
1141 Dommenget, D., & Yu, Y. (2017). The effects of remote SST forcings on ENSO dynamics,
1142 variability and diversity. *Climate Dynamics*, *49*(7), 2605-2624.
1143 Fang, X., & Chen, N. (2023). Quantifying the predictability of ENSO complexity using a
1144 statistically accurate multiscale stochastic model and information theory. Journal of
1145 Climate, 36(8), 2681-2702.

1146 Fang, X. H., & Mu, M. (2018). A three-region conceptual model for central Pacific El Niño
1147 including zonal advective feedback. *Journal of Climate*, *31*(13), 4965-4979.
1148 Fang, X. H., & Zheng, F. (2021). Effect of the air–sea coupled system change on the ENSO
1149 evolution from boreal spring. *Climate Dynamics*, *57*(1-2), 109-120.
1150 Fedorov, A. V. (2010). Ocean response to wind variations, warm water volume, and simple
1151 models of ENSO in the low-frequency approximation. *Journal of climate*, *23*(14), 3855-
1152 3873.
1153 Frauen, C., and D. Dommenget (2012), Influ- ences of the tropical Indian and Atlantic Oceans
1154 on the predictability of ENSO, Geophys. Res. Lett., 39, L02706, doi:10.1029/
1155 2011GL050520.
1156 Gadgil, S., Joseph, P. V., & Joshi, N. V. (1984). Ocean–atmosphere coupling over monsoon
1157 regions. *Nature*, *312*(5990), 141-143.
1158 Geng, T., Cai, W., & Wu, L. (2020). Two types of ENSO varying in tandem facilitated by
1159 nonlinear atmospheric convection. *Geophysical Research Letters*, *47*, e2020GL088784.
1160 https://doi. org/10.1029/2020GL088784
1161 Graham, F. S., Brown, J. N., Wittenberg, A. T., & Holbrook, N. J. (2015). Reassessing
1162 conceptual models of ENSO. *Journal of Climate*, *28*(23), 9121-9142.
1163 Graham, F. S., Wittenberg, A. T., Brown, J. N., Marsland, S. J., & Holbrook, N. J. (2017).
1164 Understanding the double peaked El Niño in coupled GCMs. *Climate Dynamics*, *48*(5-6),
1165 2045-2063.
1166 Hasegawa, T., T. Horii, and K. Hanawa (2006), Two different features of discharge of
1167 equatorial upper ocean heat content related to El Niño events, Geophys. Res. Lett., 33,
1168 L02609, doi:10.1029/2005GL024832.
1169 Hayashi, M., F.-F. Jin, and M. F. Stuecker, 2020: Dynamics for El Niño-La Niña asymmetry
1170 constrain equatorial-Pacific warming pattern. *Nat Commun*, **11**, 4230,
1171 https://doi.org/10.1038/s41467-020-17983-y.
1172 Iwakiri, T., and M. Watanabe, 2022: Multiyear ENSO Dynamics as Revealed in Observations,
1173 Climate Model Simulations, and the Linear Recharge Oscillator. Journal of Climate, 35,
1174 4025-4042, https://doi.org/10.1175/JCLI-D-22-0108.1.
1175 Izumo T (2003) The equatorial undercurrent and associated mass and heat exchanges in the
1176 tropical Pacific: variability, links with El Niño–La Niña events. Ph.D. manuscript,
1177 available at http:// tel.ccsd.cnrs.fr

1178 Izumo, T. (2005). The equatorial undercurrent, meridional overturning circulation, and their
1179 roles in mass and heat exchanges during El Niño events in the tropical Pacific
1180 Ocean. *Ocean Dynamics*, *55*(2), 110-123.
1181 Izumo, T., Vialard, J., Lengaigne, M., de Boyer Montegut, C., Behera, S. K., Luo, J. J., ... &
1182 Yamagata, T. (2010). Influence of the state of the Indian Ocean Dipole on the following
1183 year's El Niño. *Nature Geoscience*, *3*(3), 168-172.
1184 Izumo, T., Lengaigne, M., Vialard, J., Luo, J. J., Yamagata, T., & Madec, G. (2014). Influence
1185 of Indian Ocean Dipole and Pacific recharge on following year's El Niño: interdecadal
1186 robustness. *Climate dynamics*, *42*(1-2), 291-310.
1187 Izumo, T., Vialard, J., Dayan, H., Lengaigne, M., & Suresh, I. (2016). A simple estimation of
1188 equatorial Pacific response from windstress to untangle Indian Ocean Dipole and Basin
1189 influences on El Niño. *Climate dynamics*, *46*(7-8), 2247-2268.
1190 Izumo, T., Khodri, M., Lengaigne, M., & Suresh, I. (2018). A subsurface Indian Ocean dipole
1191 response to tropical volcanic eruptions. Geophysical Research Letters, 45(17), 9150–
1192 9159. https://doi.org/10.1029/2018GL078515
1193 Izumo, T., Lengaigne, M., Vialard, J., Suresh, I., & Planton, Y. (2019). On the physical
1194 interpretation of the lead relation between Warm Water Volume and the El Niño
1195 Southern Oscillation. *Climate Dynamics*, *52*(5), 2923-2942.
1196 Izumo, T., Vialard, J., Lengaigne, M., & Suresh, I. (2020). Relevance of relative sea surface
1197 temperature for tropical rainfall interannual variability. *Geophysical Research*
1198 *Letters*, *47*(3), e2019GL086182.
1199 Izumo, T., & Colin, M. (2022). Improving and harmonizing El Niño recharge indices.
1200 *Geophysical Research Letters*, *49*, e2022GL101003. https://doi.
1201 org/10.1029/2022GL101003
1202 Jin, F. F. (1997a). An equatorial ocean recharge paradigm for ENSO. Part I: Conceptual
1203 model. *Journal of the atmospheric sciences*, *54*(7), 811-829.
1204 Jin, F. F. (1997b). An equatorial ocean recharge paradigm for ENSO. Part II: A stripped-down
1205 coupled model. *Journal of Atmospheric Sciences*, *54*(7), 830-847.
1206 Jin, F. F., & An, S. I. (1999). Thermocline and zonal advective feedbacks within the equatorial
1207 ocean recharge oscillator model for ENSO. *Geophysical research letters*, *26*(19), 2989-
1208 2992.
1209 Jin, F.- F., Lin, L., Timmermann, A., & Zhao, J. (2007). Ensemble- mean dynamics of the
1210 ENSO recharge oscillator under state- dependent stochastic forcing. *Geophysical*
1211 *Research Letters*, *34*(3), L03807. https://doi.org/10.1029/2006GL027372

Jin, F. F., Chen, H. C., Zhao, S., Hayashi, M., Karamperidou, C., Stuecker, M. F., ... & Geng, L. (2020). Simple ENSO models. *El Niño Southern Oscillation in a Changing Climate*, 119-151.

Johnson, N. C., & Xie, S.- P. (2010). Changes in the sea surface temperature threshold for tropical convection. *Nature Geoscience*, *3*(12), 842–845. https://doi.org/10.1038/ngeo1008

Johnson, N. C., & Kosaka, Y. (2016). The impact of eastern equatorial Pacific convection on the diversity of boreal winter El Niño teleconnection patterns. *Climate Dynamics*, *47*(12), 3737-3765.

Jourdain NC, Lengaigne M, Vialard J, Izumo T, Gupta AS (2016) Fur- ther insights on the influence of the Indian Ocean dipole on the following year's ENSO from observations and CMIP5 models. J Clim 29(2):637–658. https://doi.org/10.1175/JCLI-D-15-0481.1

Keane, A., Krauskopf, B., & Postlethwaite, C. (2016). Investigating irregular behavior in a model for the El Niño Southern Oscillation with positive and negative delayed feedback. *SIAM Journal on Applied Dynamical Systems*, *15*(3), 1656-1689.

Kosaka, Y., & Xie, S. P. (2013). Recent global-warming hiatus tied to equatorial Pacific surface cooling. *Nature*, *501*(7467), 403-407.

Kug, J. S., & Kang, I. S. (2006). Interactive feedback between ENSO and the Indian Ocean. *Journal of climate*, *19*(9), 1784-1801.

Kug, J. S., Jin, F. F., & An, S. I. (2009). Two types of El Niño events: cold tongue El Niño and warm pool El Niño. *Journal of climate*, *22*(6), 1499-1515.

Kug, J.-S., Choi, J., An, S.-I., Jin, F.-F., and Wittenberg, A. T. (2010). Warm Pool and Cold Tongue El Niño Events as Simulated by the GFDL 2.1 Coupled GCM. J. Clim. 23, 1226–1239. doi:10.1175/2009JCLI3293.1

Lai AWC, Herzog M, Graf HF (2015) Two key parameters for the El Niño continuum: zonal wind anomalies and Western Pacific sub- surface potential temperature. Clim Dyn 45(11–12):3461–3480. https://doi.org/10.1007/s00382-015-2550-0

Lengaigne M, Boulanger J-P, Menkes C, Spencer H (2006) Influence of the seasonal cycle on the termination of El Niño events in a coupled general circulation model. J Clim 19(9):1850–1868. https ://doi.org/10.1175/JCLI3706.1

Linz M, Tziperman E, MacMartin DG (2014) Process-based analysis of climate model ENSO simulations: intermodel consistency and compensating errors. J Geophys Res 119:7396–7409. https://doi. org/10.1002/2013JD021415

1245 Lloyd J, Guilyardi E, Weller H (2010) The role of atmosphere feed- backs during ENSO in the
1246 CMIP3 models. Part II: using AMIP runs to understand the heat flux feedback
1247 mechanisms. Clim Dyn 37:1271–1292. https://doi.org/10.1007/s00382-010-0895-y
1248 Lu, B., Jin, F. F., & Ren, H. L. (2018). A coupled dynamic index for ENSO
1249 periodicity. *Journal of Climate*, *31*(6), 2361-2376.
1250 Luo J-J, Zhang R, Behera S, Masumoto Y, Jin F-F, Lukas R, Yamagata T (2010) Interaction
1251 between El Niño and extreme Indian Ocean Dipole. J Clim 23:726–742
1252 McCreary, J. P., & Lu, P. (1994). Interaction between the subtropical and equatorial ocean
1253 circulations: The subtropical cell. *Journal of Physical Oceanography*, *24*(2), 466-497.
1254 McPhaden, M. J. (2012). A 21st century Shift in the Relationship between ENSO SST and
1255 Warm Water Volume Anomalies. Geophys. Res. Lett. 39, a–n. doi:10.
1256 1029/2012GL051826
1257 Meinen CS, McPhaden MJ (2000) Observations of warm water volume changes in the
1258 equatorial Pacific and their relationship to El Niño and La Niña. J Clim 13:3551–3559
1259 Menkes CE, Lengaigne M, Marchesiello P, Jourdain NC, Vincent EM, Lefèvre J, Chauvin F,
1260 Royer JF. Comparison of tropical cyclogenesis indices on seasonal to interannual
1261 timescales. Climate dynamics. 2012 Jan;38:301-21.
1262 Neelin, J. D., Battisti, D. S., Hirst, A. C., Jin, F. F., Wakata, Y., Yamagata, T., & Zebiak, S. E.
1263 (1998). ENSO theory. *Journal of Geophysical Research: Oceans*, *103*(C7), 14261-
1264 14290.
1265 Okumura, Y. M. (2019). ENSO diversity from an atmospheric perspective. *Current Climate*
1266 *Change Reports*, *5*(3), 245-257.
1267 Picaut, J., Ioualalen, M., Menkès, C., Delcroix, T., & Mcphaden, M. J. (1996). Mechanism of
1268 the zonal displacements of the Pacific warm pool: Implications for
1269 ENSO. *Science*, *274*(5292), 1486-1489.
1270 Picaut J, Masia F, du Penhoat Y (1997) An advective–reflective con- ceptual model for the
1271 oscillatory nature of the ENSO. Science 277:663–666.
1272 https://doi.org/10.1126/science.277.5326.663
1273 Planton, Y., Vialard, J., Guilyardi, E., Lengaigne, M., & Izumo, T. (2018). Western Pacific
1274 oceanic heat content: A better predictor of La Niña than of El Niño. *Geophysical*
1275 *Research Letters*, *45*(18), 9824-9833.
1276 Power, S. B. (2011). Simple analytic solutions of the linear delayed-action oscillator equation
1277 relevant to ENSO theory. *Theoretical and applied climatology*, *104*(1), 251-259.

1278 Praveen Kumar, B., Jérôme Vialard, Matthieu Lengaigne, V. S. N. Murty, Michael J.
1279 Mcphaden, M. F. Cronin, Françoise Pinsard, and K. Gopala Reddy. "TropFlux wind
1280 stresses over the tropical oceans: evaluation and comparison with other
1281 products." *Climate dynamics* 40 (2013): 2049-2071.
1282 Giese, B. S., & Ray, S. (2011). El Niño variability in simple ocean data assimilation (SODA),
1283 1871–2008. *Journal of Geophysical Research: Oceans*, *116*(C2).
1284 Ren, H.-L., and Jin, F.-F. (2013). Recharge Oscillator Mechanisms in Two Types of ENSO. J.
1285 Clim. 26, 6506–6523. doi:10.1175/jcli-d-12-00601.1
1286 Ren, H., and R. Wang, 2020: Distinct Growth Rates of the Two ENSO Types. Geophys. Res.
1287 Lett., 47, https://doi.org/10.1029/2020GL088179.
1288 Santoso, A., Mcphaden, M. J., & Cai, W. (2017). The defining characteristics of ENSO extremes
1289 and the strong 2015/2016 El Niño. Reviews of Geophysics, 55, 1079–1129. https://doi.
1290 org/10.1002/2017RG000560
1291 Shin, N. Y., Kug, J. S., Stuecker, M. F., Jin, F. F., Timmermann, A., & Kim, G. I. (2022). More
1292 frequent central Pacific El Niño and stronger eastern pacific El Niño in a warmer
1293 climate. *npj Climate and Atmospheric Science*, *5*(1), 101.
1294 Srinivas G, Vialard J, Lengaigne M, Izumo T, Guilyardi E. Relative contributions of sea surface
1295 temperature and atmospheric nonlinearities to ENSO asymmetrical rainfall response.
1296 Journal of Climate. 2022 Jun 15;35(12):3725-45.
1297 Srinivas G, Vialard J, Liu F, Voldoire A, Izumo T, Guilyardi E, Lengaigne M,. Dominant
1298 contribution of atmospheric non-linearities to ENSO asymmetry and extreme El Niño
1299 events. Sci. Reports, under revision, 2024.
1300 Stellema A, Sen Gupta A, Taschetto AS and Feng M (2022) Pacific Equatorial Undercurrent:
1301 Mean state, sources, and future changes across models. *Front. Clim.* 4:933091. doi:
1302 10.3389/fclim.2022.933091
1303 Stuecker, M. F., Timmermann, A., Jin, F. F., McGregor, S., & Ren, H. L. (2013). A
1304 combination mode of the annual cycle and the El Niño/Southern Oscillation. *Nature*
1305 *Geoscience*, *6*(7), 540-544.
1306 Suarez MJ, Schopf PS (1988) A delayed action oscillator for ENSO. J Atmos Sci 45:3283–
1307 3287
1308 Sullivan A, Luo JJ, Hirst AC, Bi D, Cai W, He J. Robust contribution of decadal anomalies to
1309 the frequency of central-Pacific El Niño. Scientific reports. 2016 Dec 5;6(1):38540.

1310 Takahashi K, Montecinos A, Goubanova K, Dewitte B (2011) ENSO regimes: reinterpreting
1311 the canonical and Modoki El Niño. Geo- phys Res Lett 38:1–5.
1312 https://doi.org/10.1029/2011GL047364
1313 Takahashi, K., Karamperidou, C., & Dewitte, B. (2019). A theoretical model of strong and
1314 moderate El Niño regimes. *Climate Dynamics, 52*(12), 7477–7493.
1315 https://doi.org/10.1007/s00382-018-4100-z
1316 Timmermann, Axel, et al. "El Niño–southern oscillation complexity." *Nature* 559.7715 (2018):
1317 535-545.
1318 Tippett MK, Camargo SJ, Sobel A (2011) A poisson regression index for tropical cyclone
1319 genesis and the role of large-scale vorticity in genesis. J clim.
1320 doi:10.1175/2010JCLI3811.1, accepted
1321 Thual, S. and Dewitte, B., 2023: The role of spatial shifting in El Niño/Southern Oscillation
1322 complexity, accepted.
1323 Thual, S., B. Dewitte, N. Ayoub, and O. Thual, 2013: An Asymptotic Expansion for the
1324 Recharge-Discharge Model of ENSO, J. Phys. Oceanogr., 43, 1407–1416.
1325 Trenberth KE, Stepaniak DP. Indices of el Niño evolution. Journal of climate. 2001 Apr
1326 15;14(8):1697-701.
1327 Tziperman, E., Cane, M. A., & Zebiak, S. E. (1995). Irregularity and locking to the seasonal
1328 cycle in an ENSO prediction model as explained by the quasi-periodicity route to
1329 chaos. *Journal of Atmospheric Sciences*, *52*(3), 293-306.
1330 Van Oldenborgh, G. J., Hendon, H., Stockdale, T., L'Heureux, M., De Perez, E. C., Singh, R.,
1331 & Van Aalst, M. (2021). Defining El Niño indices in a warming climate. *Environmental*
1332 *Research Letters*, *16*(4), 044003.
1333 Vecchi, G. A., & Soden, B. J. (2007). Effect of remote sea surface temperature change on
1334 tropical cyclone potential intensity. Nature, 450(7172), 1066–1070.
1335 https://doi.org/10.1038/nature06423
1336 Vialard, J., Menkes, C., Boulanger, J. P., Delecluse, P., Guilyardi, E., McPhaden, M. J., &
1337 Madec, G. (2001). A model study of oceanic mechanisms affecting equatorial Pacific sea
1338 surface temperature during the 1997–98 El Niño. *Journal of Physical*
1339 *Oceanography*, *31*(7), 1649-1675.
1340 Vijayeta, A., and D. Dommenget, 2018: An evaluation of ENSO dynamics in CMIP
1341 simulations in the framework of the recharge oscillator model. Clim Dyn, 51, 1753-
1342 1771, https://doi.org/10.1007/s00382-017-3981-6.

Vincent, E. M., Lengaigne, M., Menkes, C. E., Jourdain, N. C., Marchesiello, P., & Madec, G. (2011). Interannual variability of the South Pacific Convergence Zone and implications for tropical cyclone genesis. *Climate dynamics*, *36*, 1881-1896.

Wang, C., & Picaut, J. (2004). Understanding ENSO physics—A review. *Earth's Climate: The Ocean–Atmosphere Interaction, Geophys. Monogr*, *147*, 21-48.

Wang, C. (2001). A unified oscillator model for the El Niño–Southern Oscillation. *Journal of Climate*, *14*(1), 98-115.

Wang, R., and H.-L. Ren, 2017: The linkage between two ENSO types/modes and the interdecadal changes of ENSO around the year 2000. Atmospheric and Oceanic Science Letters, 10, 168-174, https://doi.org/10.1080/16742834.2016.1258952.

Williams, I. N., & Patricola, C. M. (2018). Diversity of ENSO events unified by convective threshold sea surface temperature: A nonlinear ENSO index. *Geophysical Research Letters*, *45*(17), 9236-9244.

Wyrtki K (1985) Water displacements in the Pacific and the genesis of El Niño cycles. J Geophys Res 90:7129–7132

Xie R, Huang F, Jin FF, Huang J. The impact of basic state on quasi-biennial periodicity of central Pacific ENSO over the past decade. Theoretical and Applied Climatology. 2015 Apr;120:55-67.

Yu et al. (2015; they combine a recharge oscillator to a slab ocean coupled to an AGCM to capture ENSO dynamics and diversity

Zeller M, McGregor S, Spence P. Hemispheric asymmetry of the Pacific shallow meridional overturning circulation. Journal of Geophysical Research: Oceans. 2019 Aug;124(8):5765-86

Zeller M, McGregor S, van Sebille E, Capotondi A, Spence P. Subtropical-tropical pathways of spiciness anomalies and their impact on equatorial Pacific temperature. Climate Dynamics. 2021 Feb;56(3-4):1131-44.

Zhang, W., Li, S., Jin, F.- F., Xie, R., Liu, C., Stuecker, M. F., & Xue, A. (2019). ENSO regime changes responsible for decadal phase relationship variations between ENSO sea surface temperature and warm water volume. Geophysical Research Letters, 46, 7546–7553. https://doi.org/ 10.1029/2019GL082943

Zhu, X., Greatbatch, R. J., & Claus, M. (2017). Interannual variability of tropical Pacific sea level from 1993 to 2014. *Journal of Geophysical Research: Oceans*, *122*(1), 602-616.

Supplementary Information for

The hybrid Recharge Delayed Oscillator: a more realistic El Niño conceptual model

Takeshi Izumo,[a,b] Maxime Colin,[c,d,e] Fei-Fei Jin,[f] and Bastien Pagli,[a]

[a] *Institut de Recherche pour le Développement (IRD), UMR241 SECOPOL (ex-EIO) laboratory, Université de la Polynésie Française (UPF), Tahiti, French Polynesia*
[b] *formerly at IRD, Sorbonne Université - CNRS-IRD-MNHN, LOCEAN Laboratory, IPSL, Paris, France*
[c] *Climate Change Research Centre, University of New South Wales, Sydney, New South Wales, Australia*
[d] *Laboratoire GEPASUD, University of French Polynesia, Tahiti, French Polynesia*
[e] *now at Leibniz Centre for Tropical Marine Research (ZMT), Bremen, Germany*
[f] *Department of Atmospheric Sciences, University of Hawai'i at Mānoa, Honolulu, HI, United States*

Submitted to Journal of Climate on March 3rd, 2023
Revised, September 6th, 2023
Revised, January 18th, 2024

Corresponding author: Takeshi Izumo, takeshi.izumo@ird.fr

Supplementary text S1: Additional data and methods information

a. Validation of indices (sensitivity tests)

Using Niño3 region instead of Niño3.4 region leads to qualitatively-similar results. It leads to only a weak decrease for RDO temperature equation skill (see RDO equations in section 3), and a slight F_1 increase, for instance in obs2 from 0.11 to 0.12±0.02 month^{-1} and a β decrease from 0.09 to 0.07±0.02 month^{-1} as expected physically because Niño3 is slightly further east (cf. Fig. 2a and Suppl. Fig. S1).

For the recharge index, the debate is partly caused by the potentially-misleading character of the most commonly used recharge index, the equatorial Pacific OHC index, h_{eq}, which mixes the slow recharge mode with the temporary rapid variations related to equatorial Kelvin waves that project strongly onto h_{eq}, as shown by Izumo et al. (2018a). Through an objective approach to optimize the fit of the RO differential equations with observations, Izumo and Colin (2022) have thus developed a more physical and optimized index of the ENSO slow recharge mode, uncorrelated to T_E (i.e. independent of the fast adjustment mode). They separate the fast oceanic adjustment in phase with T_E (tilt mode) and the slow oceanic component out of phase with T_E, i.e. the pure recharge/discharge process (whose tendency is forced by in-phase currents associated to T_E). Doing this separation allows them to reconcile western and equatorial recharge indices, as well as SLA, Z20 or OHC-based indices, as all the recharge indices become much more similar when only looking at their pure recharge components independent of T_E. The study also investigates what is the best averaging region optimizing the RO set of equations. The optimal two-rectangle region to capture the slow recharge process is obtained by adding a h_{sw} southwest Pacific box to h_{eq} box (see Fig. 1b that physically represents the recharge after long-lasting easterly anomalies in observations; see Iwakiri and Watanabe 2022 for processes driving long-lasting La Niña). This recharge (in the case of easterly anomalies, discharge in the westerly case) is through (1) an equatorial basin adjustment with the leakage of OHC negative anomalies towards the poles along the eastern boundary recharging equatorial OHC (e.g. Izumo et al. 2018, their Supplementary Figure S4) and (2) meridionally-asymmetric Ekman pumping recharging more the southwest Pacific, that will progressively favor positive T_E and thus El Niño onset (this asymmetry explains why the optimal region, "eq+sw", is asymmetric). Adding "sw" to "eq" further improves the fit of RO equations and ENSO hindcasts, with the added advantage of reducing the correlation to T_E. Note that this eq+sw region is actually also optimal for the RDO set of equations developed in the present study (not shown). Note also that one

could also use the 20ºC isotherm depth, the Z20, instead of SLA, but the SLA is directly observed by satellite and more easily available in CMIP database and gives equivalent results. In fine, the optimized recharge index statistically-independent from T_E is $h_{ind\_eq+sw} = h_{eq+sw} - K T_E \approx h_{eq+sw}$ (Izumo and Colin 2022).

Indeed, the RDO equations 6 and 7 remain in practice quasi-similar if we use h_{eq+sw} instead of h_{ind_eq+sw} for the recharge index. As K is so small, the shared variance between h_{eq+sw} and T_E is for instance only 9% for obs2. Hence I.e. β (e.g. 0.09±0.02 month^{-1} in obs2) remains mathematically identical. F_1 does not change at the second digit, remaining for instance in obs2 at 0.11±0.02 month^{-1}. F_2 changes weakly, from 0.16±0.02 to 0.17±0.02 month^{-1}. Only R and ε decrease, R from 0.03±0.02 to 0.00±0.02 month^{-1} and ε from 0.00±0.02 to -0.05±0.02 month^{-1} in obs2 for instance. The correlation skill for the temperature equation remains mathematically identical, and the skill for recharge equation decreases slightly, e.g. from 0.68 to 0.66 in obs2.

b. Methods

Here we use typical statistical methods. The monthly seasonal cycle (computed by averaging each month of the year over the whole period) is removed and intraseasonal variations are filtered out by a 4-month window Hanning filter, so that periods lower than ~2-month are removed (considering as fast adjustments anything with timescales less than ~2-month). For the long historical datasets 'obs2' (ORAS5 analysis over its whole extended period 1959-2018 + HadiSST), hist (SODA2.2.6 + HadiSST, note: at the time of doing the present research work, CERA20C ECMWF server was unfortunately down, and could not be used) and CMIP, we use in addition to the intraseasonal low-pass filter a high-pass Hanning filter (14-year window) to remove interdecadal variability with cutting frequency at periods of ~10-year, as our focus is here on ENSO main interannual timescale (note that interdecadal variability and possible trends are removed to be safe, but the results are quasi-similar without this high-pass filter).

Multivariate linear regressions are used to obtain the best-fit coefficients for the RDO differential equations. Note that for monthly values, it is important to use centered derivatives to estimate h and T_E tendencies accurately (using forward derivatives leads to biased parameters and thus biases of the RDO response to stochastic forcing). All along the paper, numbers are given for normalized h and T_E, i.e. divided by their standard deviation (STD), so as to represent typical amplitudes. Using formulae (30) of Bretherton et al. (1999), we have about one effective degree of freedom every 4 months, i.e. ~85 for obs1, ~140 for obs2, ~370 for hist, ~360 for

each CMIP5 model historical run, ~450 for each CMIP6 historical run. These effective numbers of degrees of freedom are sufficiently large, so that statistics are robust. For statistical significance, we can thus use typical two-tailed Student t-tests for e.g. 90% or 95% confidence intervals. As here, our effective number of degrees of freedom *dof* is sufficiently large, being always larger than ~80, the reader can easily switch from 90 to 95% [or even 99%] intervals by multiplying by the ratio of the corresponding t-values, quite stable for *dof* above 30 (e.g. for *dof*=80, ratio of 1.2 to switch from 90 to 95% [ratio of 1.6 to switch from 90 to 99%]).

To obtain the RDO response to stochastic forcing, we use the Euler-Heun numerical scheme, necessary when a multiplicative noise is included. The stochastic forcings of the RDO are red noises (except for computing the spectral response, for which we force by white noise). Their amplitudes are based on the STD of the residuals of the tendency equations regression fits. We take a realistic decorrelation time of 5-day for these red noises, which we have estimated from the observed decorrelation time of the main stochastic forcing of ENSO, namely intraseasonal zonal windstress over the oceanic equatorial wave guide (2ºN-2ºS) in the western Pacific (e.g. 120ºE-155ºW) due to westerly wind bursts and to Madden-Julian Oscillation (MJO; using daily Tropflux product; Praveen Kumar et al. 2013; interannual anomalies removed with a 6-month window Hanning filter). This decorrelation time is qualitatively consistent with the one of Vijayeta and Dommenget (2018). Note that, at the end, the amplitude of the synthetical time series directly depends on this time. The larger the decorrelation time is, the more energy there will be at interannual timescales, the larger the RDO response will be. E.g. STD increases by about 0.3 from 5-day to 15-day, for non-linear seasonal RDO based on hist shown in Section 5 (even if the STD of the red noises are unchanged).

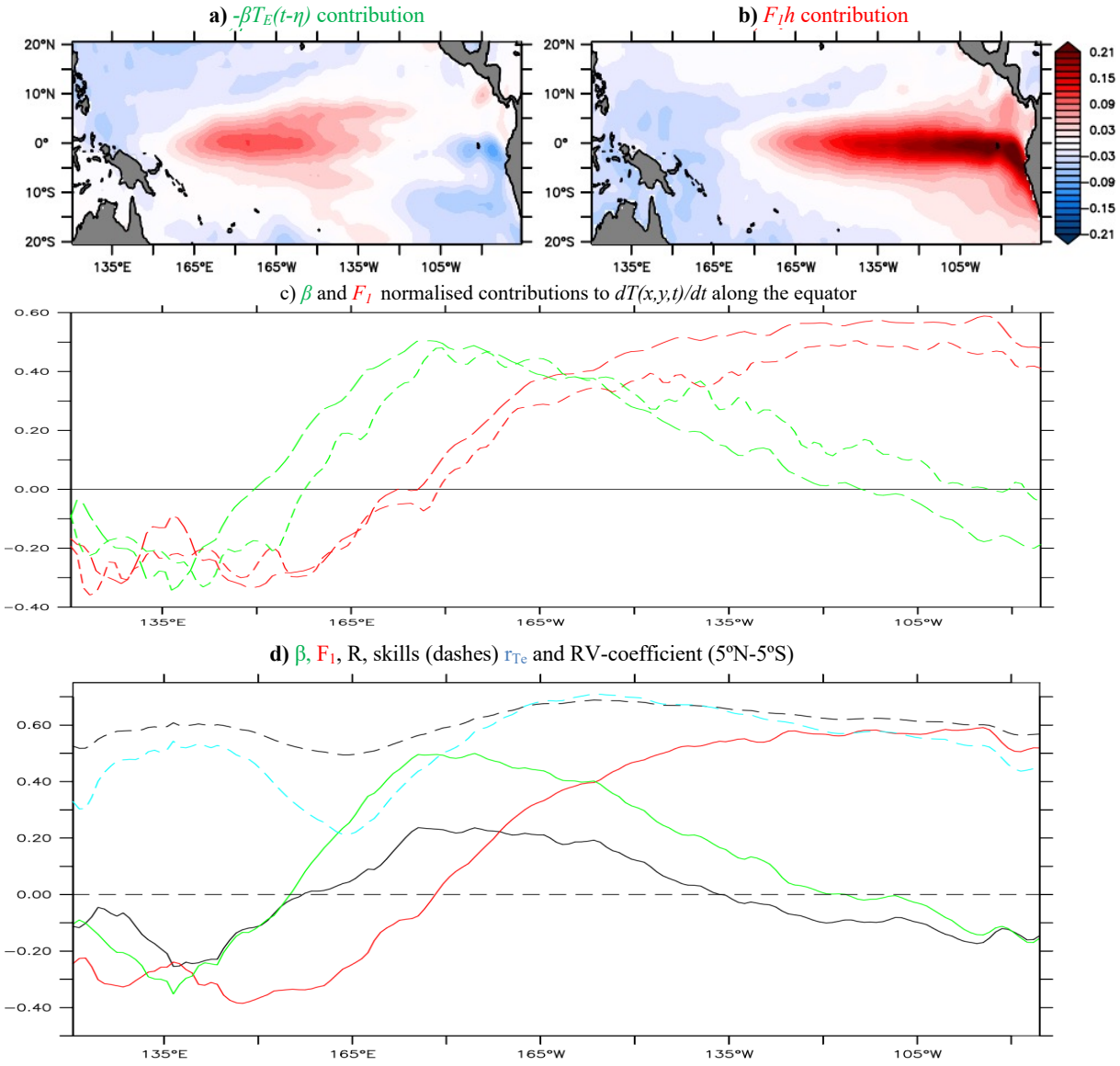

Suppl. Fig. S1. Contributions of $-\beta(x,y)T_E(t-\eta)$ and $F_1(x,y)h$ to $dT(x,y,t)/dt$. a and b) as Fig. 2ab but for obs1 (OISST+CMEMS satellite SLA, 1993-2021) instead of obs2 (HadiSST+ORAS5 SLA, 1959-2018), for verification. **c)** $\beta(x,y)$ (green) and $F_1(x,y)$ (red) along the equator (here normalized by dividing by STD($dT(x,y,t)/dt$) for a normalized comparison), for obs1 (long dashes) and obs2 (short dashes). **d)** as c, but for 5ºN-5ºS average for obs1 only, and by also showing R (black line) and the correlation skill for temperature tendency equation 8 in blue dashes, and the RV-coefficient skill for the system of the two tendency equations together (see definition in Izumo and Colin 2022). The β contribution is qualitatively close to central Pacific (CP) El Niño spatial pattern, and the F_1 contribution is closer to the eastern Pacific (EP) El Niño pattern, both in obs1 and obs2.

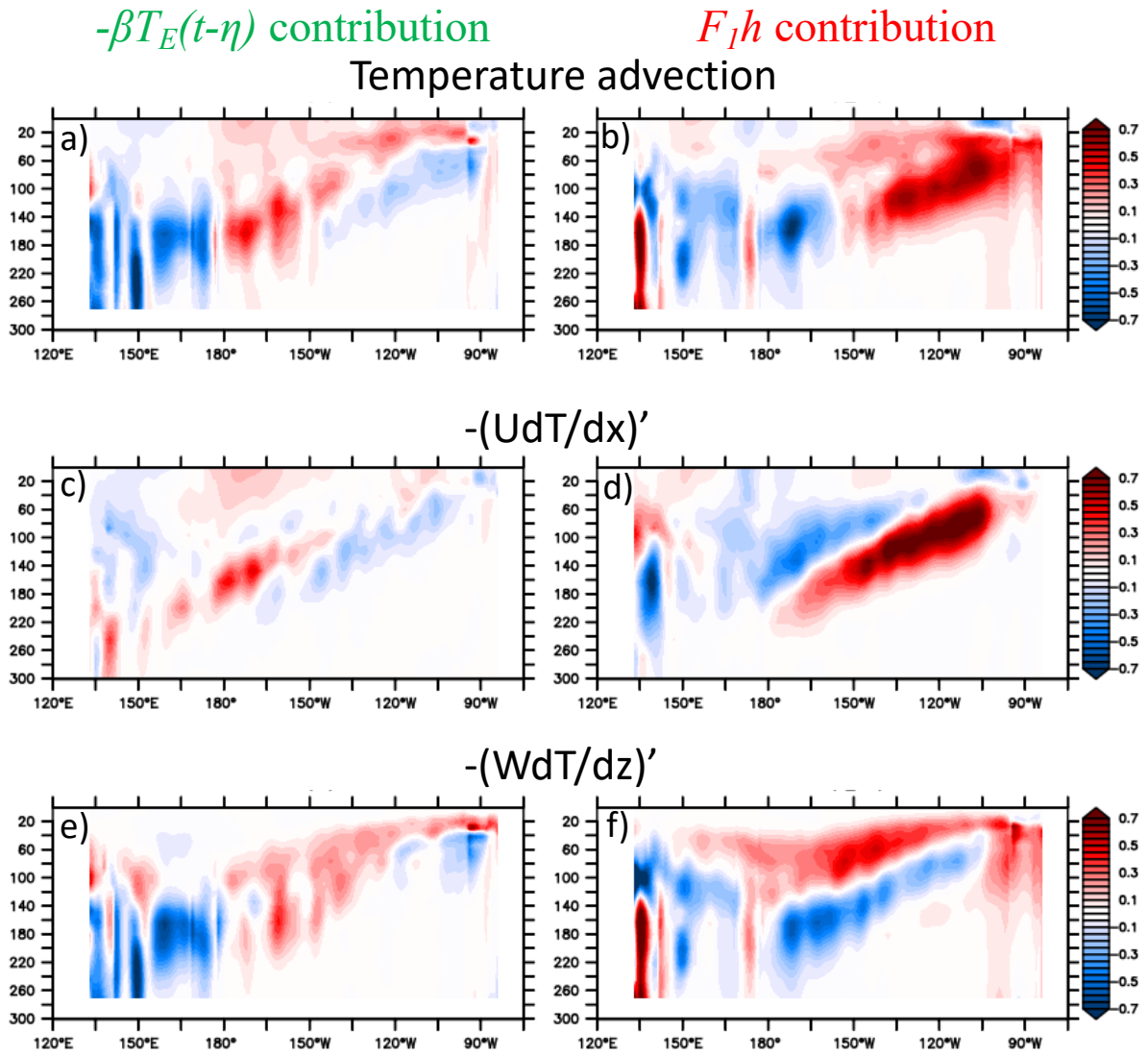

Fig. S2. Equatorial-depth section as Fig. 2efgh, but for **a,b**: the total heat advection $-U\partial T/\partial x - V\partial T/\partial y - W\partial T/\partial z$ (for monthly ORAS5, K month^{-1}); **c,d**: zonal advection $-U\partial T/\partial x$; **e,f**: vertical advection $-W\partial T/\partial z$ (sign convention: z increases upward (i.e. if e.g. z=-50 at depth 50m) and W is positive upward). The role of $-V\partial T/\partial y$ is not represented here, as it is negligible (Tropical Instability Waves (TIWs) damping effect is here not taken into account, as we only consider here monthly fields, in which TIWs are strongly filtered out). A 8°-window Hanning filter has been applied along longitude to reduce spatial noise before plotting. To interpret Fig. S2 correctly, remember that T' has much more variance around the thermocline, as even relatively-weak anomalies of the thermocline depth lead to large T' anomalies. Thus, the largest signals here are around the thermocline. Yet the weaker signals near the surface are actually essential to understand SST (and RSST) tendency (e.g. in the central Pacific on panels a and c) and should not be underestimated: they are weak in absolute amplitude but can be large in % of explained variance.

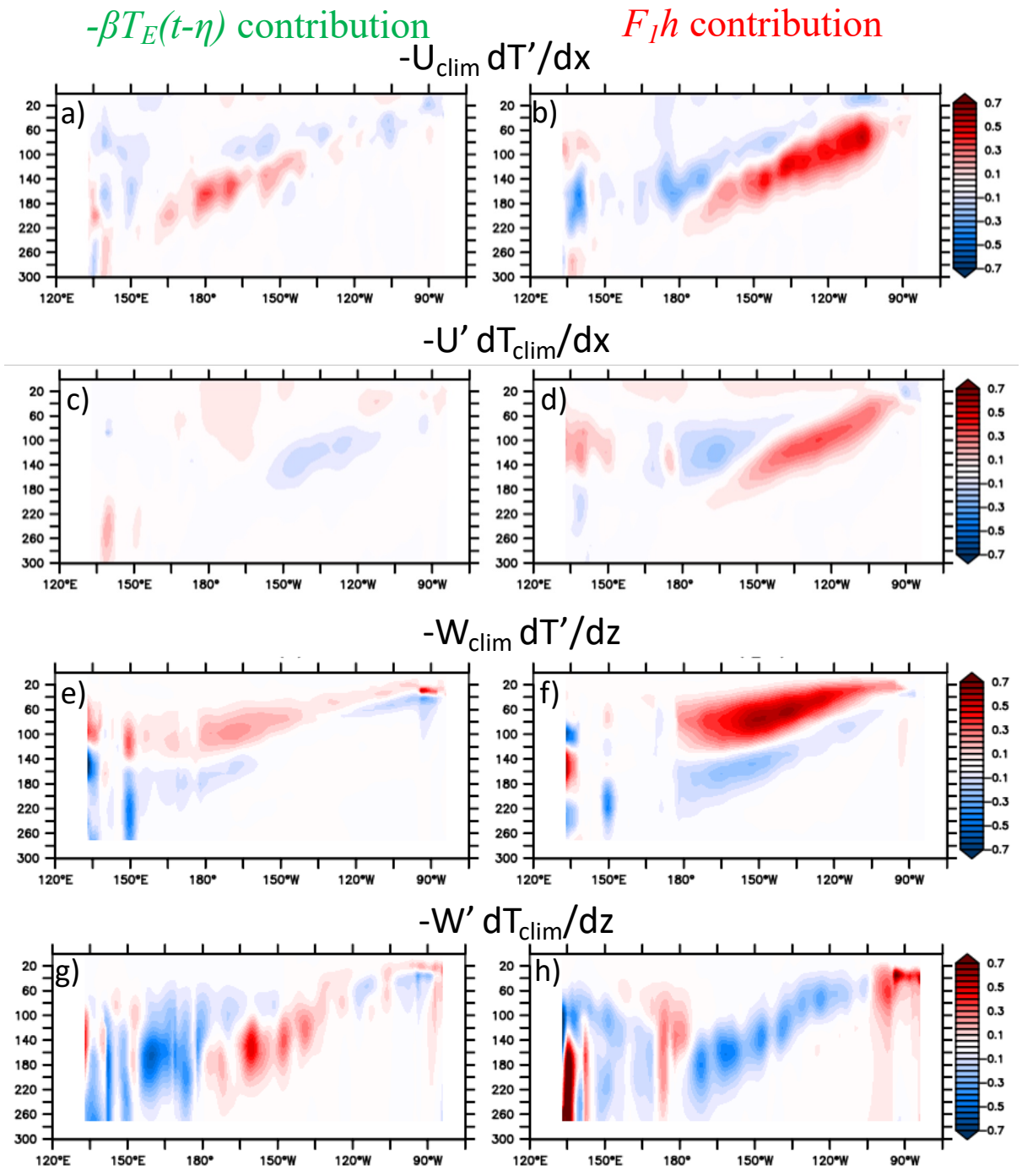

Suppl. Fig. S3. As Fig. S2, but here decomposing the zonal and vertical advections $-U\partial T/\partial x$ and $-W\partial T/\partial z$ into the contributions of anomalous current advecting climatological temperature gradient, and of anomalous temperature gradient advected by climatological current.

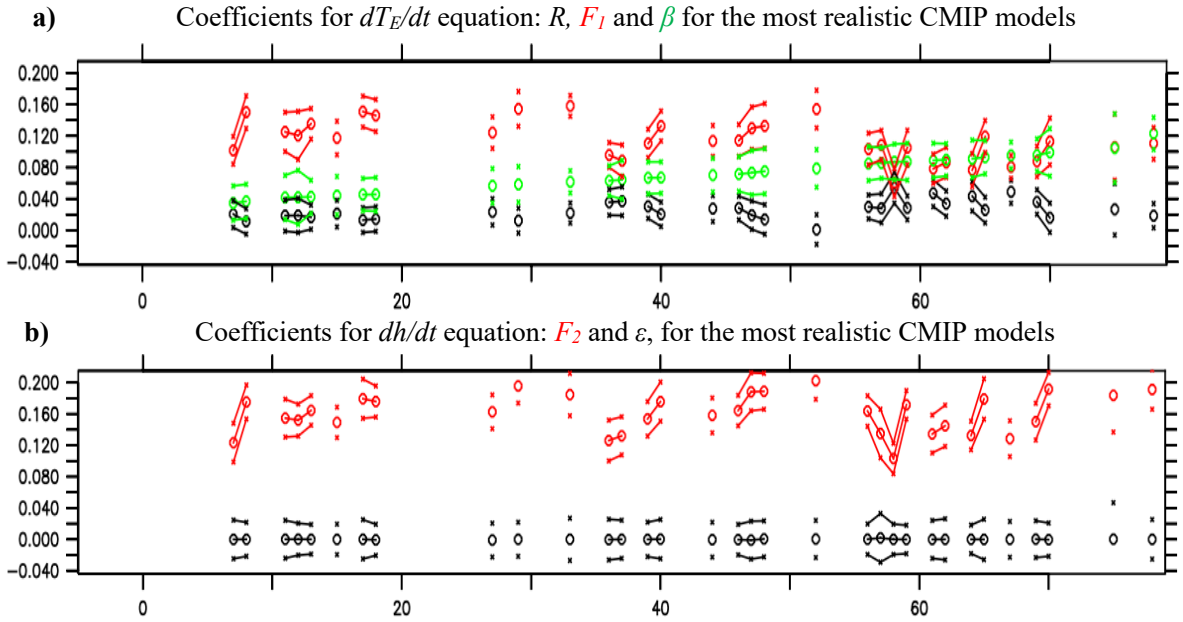

Suppl. Fig. S4. As Fig. 4 (keeping the same sorting by β), **but only for the selected most realistic CMIP models** in terms of ENSO STD and ENSO spectral shape. Both criteria have to be between 3/4 and 4/3 of their observed values (that are STD≈0.8K and spectral shape≈1.2). Interestingly, the models with the lowest β values (on the left) are rejected, as well as most models with the largest β values (on the right). The MMM of the RDO parameters for selected models (R=0.0259, F_1=0.107, β=0.072, F_2=0.161, ε=0.00 $month^{-1}$) are almost similar to the MMM for all models (R=0.0249, F_1=0.110, β=0.068, F_2=0.152, ε=0.00 $month^{-1}$). Note the slight increases in the ratio β/F_1 and in F_2 for the MMM of the selected models.

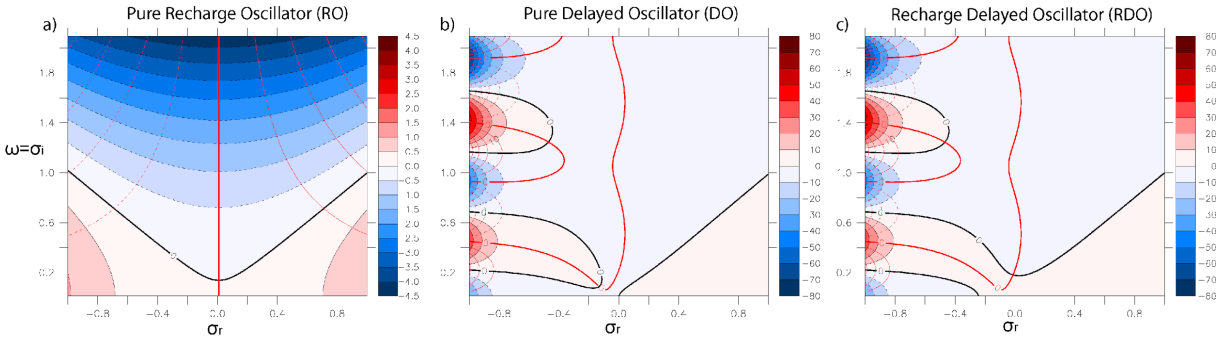

Suppl. Fig. S5. Resolution of the RDO differential equations system for solutions in $e^{\sigma t}$, by finding its eigenvalues σ which obey the characteristic equation (10): $\sigma^2 - R\sigma + \beta\sigma e^{-\sigma\eta} + F_1F_2 = 0$. Real part of the left-hand side term of equation (10) in color shading and black contours, imaginary part in red contours, as a function of σ_r along the x-axis and of σ_i along the y-axis (with $\sigma = \sigma_r + i\,\sigma_i$, its real part σ_r being the exponential growth - or damping rate if negative - and its imaginary part σ_i being the angular frequency ω, here in rad $month^{-1}$; 0.2 rad $month^{-1}$ corresponds to a period of 31.4 month). The solutions of the equation, i.e. the eigenvalues, are where both real and imaginary parts are zero, i.e. where the black and red zero-line contours intersect. Panel a is for $\beta = 0$ case (pure RO), panel b is for $F_1 = 0$ case (pure DO) and panel c is for the RDO. The RDO has an infinity of eigenmodes due to the delayed term, like the DO, while the RO only has one. RDO 1st mode is of low-frequency (period ≈ 3 years) and weakly-damped (damping rate ≈ 0.02 $month^{-1}$ ≈ 1/(4year)). RDO 2nd mode is of higher frequency (period ≈ 0.5 year) and is highly-damped (damping rate ≈ 0.45 $month^{-1}$ ≈ 1/(2months)). But this 2nd mode still adds some high-frequency response to the RDO, absent in the pure RO (cf. spectra in Fig. 7b).

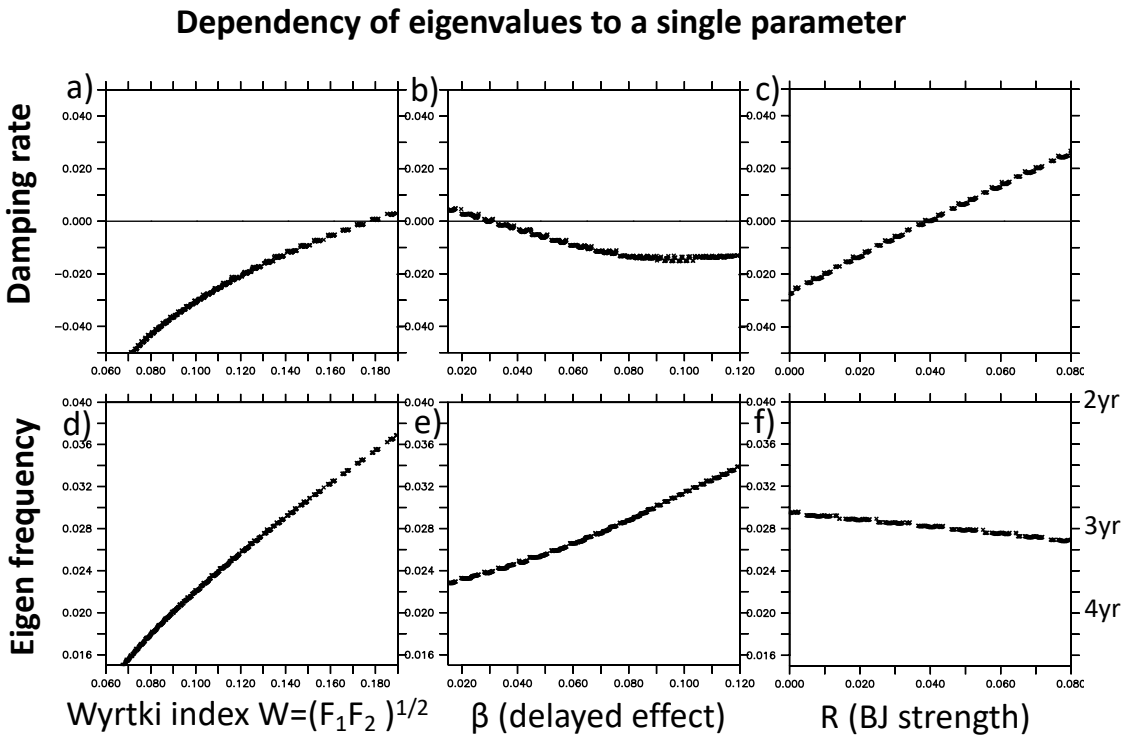

Suppl. Fig. S6. Dependency of eigenvalues to a single parameter. Dependency of RDO growth rate σ_r (upper panels) and eigenfrequency $f=\sigma_i/(2\pi)$ (lower panels) to Wyrtki angular frequency $W=(F_1F_2)^{1/2}$ (1st column), β (2nd column) and R (3rd column) separately (unit: month^{-1}).

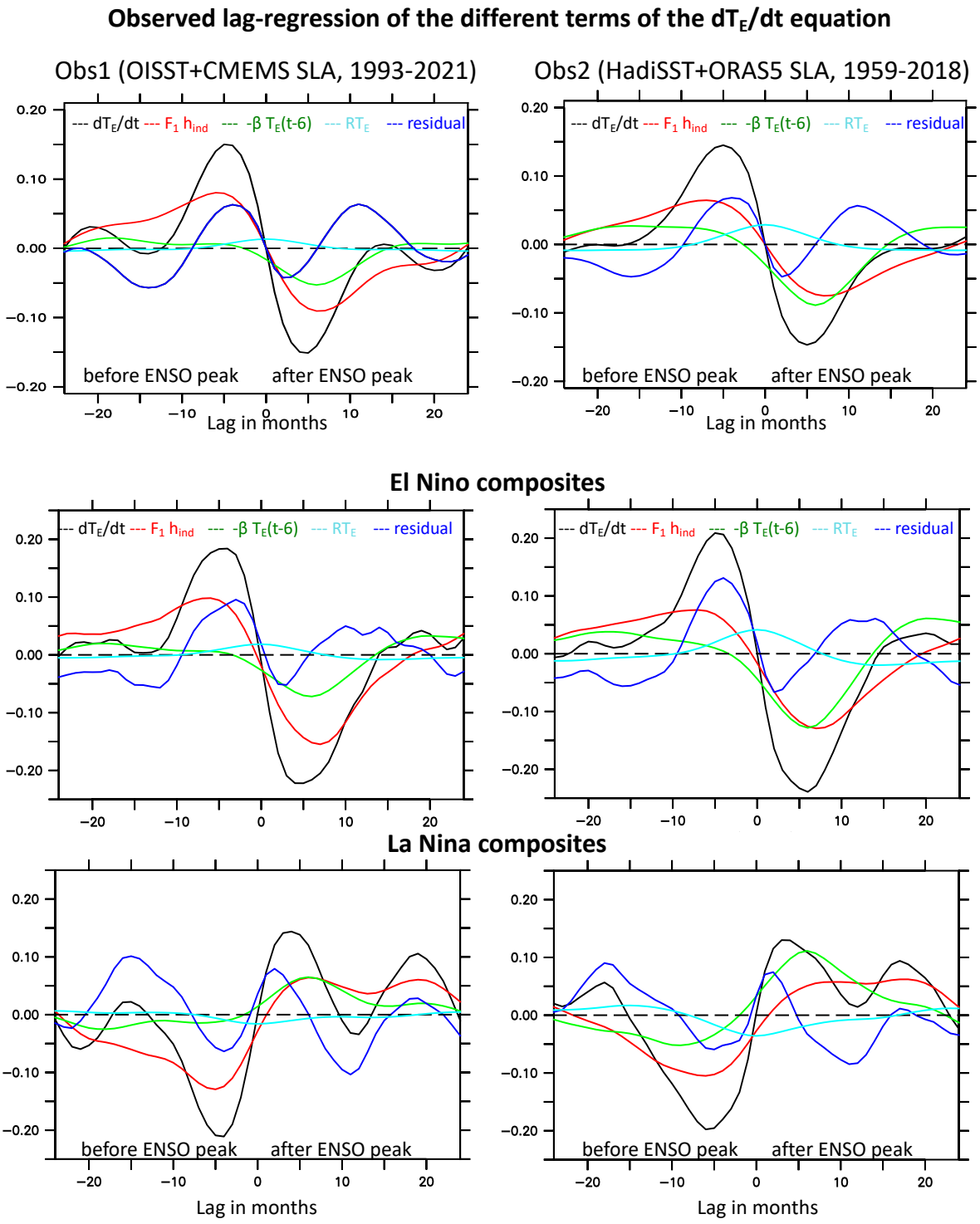

Suppl. Fig. S7. Observed lag-regression (upper row) **and lag-composites** (middle and lower rows) **of the different contributions to the T_E tendency equation.** Upper row as Fig. 7b but for obs1 and obs2. In these observations, F_1 term dominates. The residual (i.e. noise plus non-linearities notably; cf. discussion) plays also a large role. The β term plays a large role after ENSO peak, but plays a weaker role compared to RDO synthetical timeseries before ENSO peak. Middle and lower rows show El Niño and La Niña separately (composites criteria: Niño3.4 RSST anomaly larger than two thirds of its standard deviation).

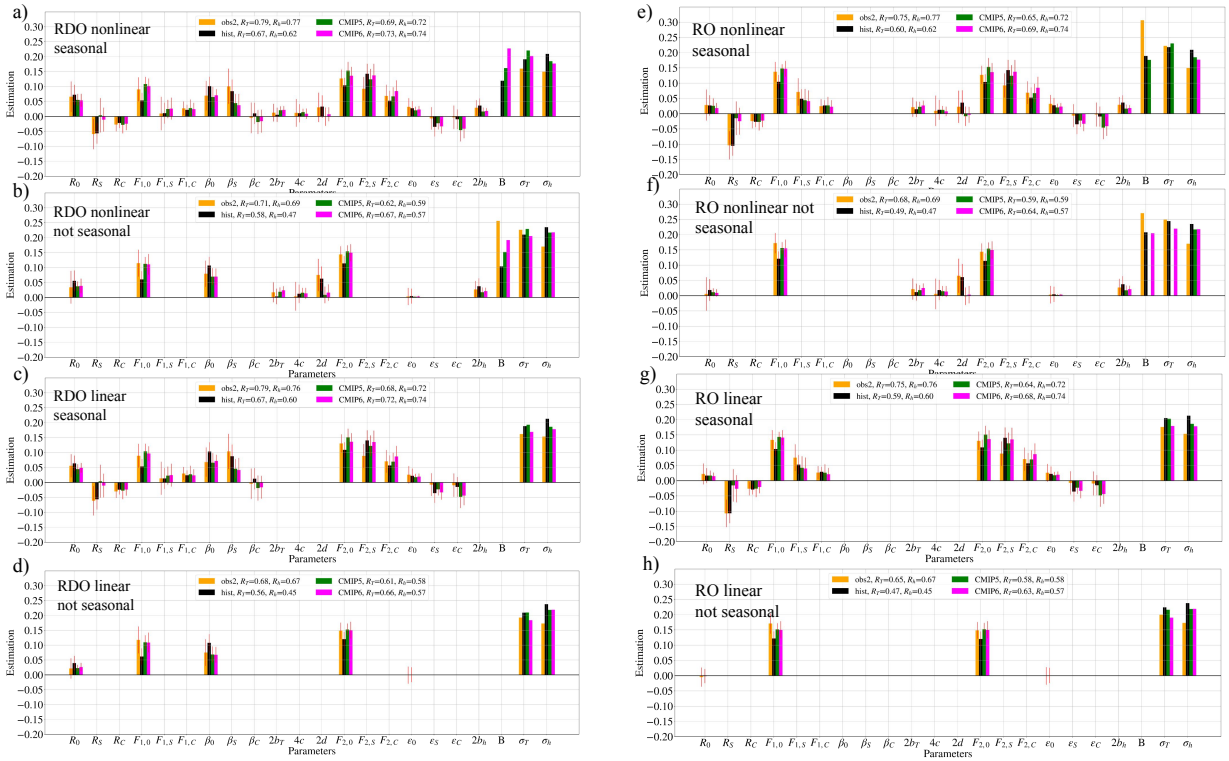

Suppl. Fig. S8. Comparison of the non-linear seasonal RDO to RO and their several versions. Bar plots as Fig. 8a, but here for both obs2 and hist, and for CMIP5 and CMIP6 separately.

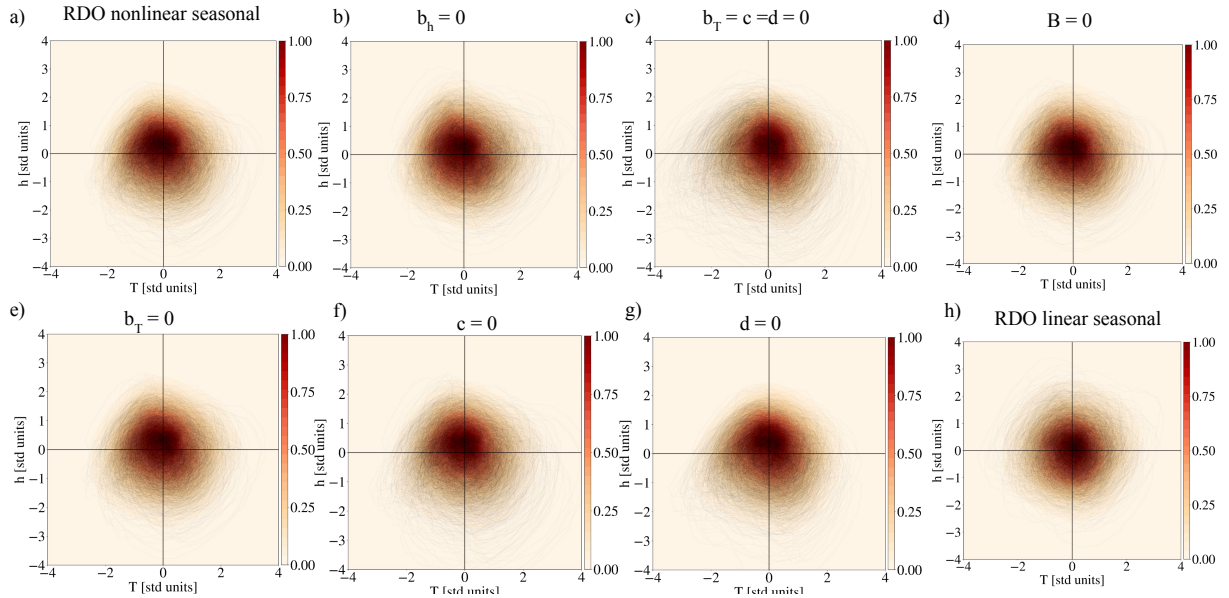

Suppl. Fig. S9. Role of each non-linear term on RDO phase diagram. Comparison of the phase diagrams of the full non-linear seasonal RDO (based on hist; shown in panel a, which is the same as Fig. 9b) with specific RDO configurations in which some non-linear terms have been artificially set to 0, to illustrate their influences.

Table S1a. CMIP5 models historical runs used in the present study (as in Izumo et al. 2019). The 32 models, for which we have SST, SLA, precipitation and windstress available in their historical runs (at least over the 1861-2005 historical period, except CanCM4 starting in 1961).

Institute name	Model name
BCC	bcc-csm1-1
	bcc-csm1-1-m
CCCma	CanCM4
	CanESM2
CMCC	CMCC-CESM
	CMCC-CM
	CMCC-CMS
CNRM-CERFACS	CNRM-CM5
	CNRM-CM5-2
CSIRO-BOM	ACCESS1-0
	ACCESS1-3
CSIRO-QCCCE	CSIRO-Mk3-6-0
FIO	FIO-ESM
INM	inmcm4
IPSL	IPSL-CM5A-LR
	IPSL-CM5A-MR
	IPSL-CM5B-LR
LASG-CESS	FGOALS-g2
LASG-IAP	FGOALS-s2
MIROC	MIROC5
	MIROC-ESM
	MIROC-ESM-CHEM
MOHC	HadGEM2-CC
MRI	MRI-CGCM3
	MRI-ESM1
NASA-GISS	GISS-E2-R
	GISS-E2-R-CC
NCC	NorESM1-M
	NorESM1-ME
NOAA-GFDL	GFDL-CM2p1
	GFDL-CM3
	GFDL-ESM2G
	GFDL-ESM2M
NSF-DOE-NCAR	CESM1-CAM5

Table S1b. The 47 CMIP6 models historical runs used in the present study (with the reference number of the historical run used).

NCC_NorESM2-MM_gn_r1i1p1f1_20191108
CCCma_CanESM5_gn_r1i1p1f1_20190429
NCC_NorCPM1_gn_r1i1p1f1_20200724
HAMMOZ-Consortium_MPI-ESM-1-2-HAM_gn_r1i1p1f1_20190627
NOAA-GFDL_GFDL-CM4_gr_r1i1p1f1_20180701
BCC_BCC-CSM2-MR_gn_r1i1p1f1_20181126
MRI_MRI-ESM2-0_gr_r1i1p1f1_20190904
INM_INM-CM5-0_gr1_r1i1p1f1_20190610
EC-Earth-Consortium_EC-Earth3-Veg-LR_gn_r1i1p1f1_20200919
NCAR_CESM2-WACCM_gr_r1i1p1f1_20190808
NASA-GISS_GISS-E2-1-G_gn_r1i1p1f1_20180827
AWI_AWI-ESM-1-1-LR_gn_r1i1p1f1_20200212
E3SM-Project_E3SM-1-1_gr_r1i1p1f1_20191204
THU_CIESM_gn_r1i1p1f1_20200220
NASA-GISS_GISS-E2-1-H_gn_r1i1p1f1_20190403
EC-Earth-Consortium_EC-Earth3-CC_gn_r1i1p1f1_20210113
NASA-GISS_GISS-E2-1-G-CC_gn_r1i1p1f1_20190815
NUIST_NESM3_gn_r1i1p1f1_20190703
CMCC_CMCC-CM2-SR5_gn_r1i1p1f1_20200616
EC-Earth-Consortium_EC-Earth3_gn_r1i1p1f1_20200918
NCC_NorESM2-LM_gn_r1i1p1f1_20190815
CSIRO-ARCCSS_ACCESS-CM2_gn_r1i1p1f1_20191108
CAS_CAS-ESM2-0_gn_r1i1p1f1_20200306
CAS_FGOALS-g3_gn_r1i1p1f1_20191107
EC-Earth-Consortium_EC-Earth3-AerChem_gn_r1i1p1f1_20200624
NCAR_CESM2_gr_r1i1p1f1_20190308
MIROC_MIROC6_gn_r1i1p1f1_20181212
NCAR_CESM2-FV2_gr_r1i1p1f1_20191120
EC-Earth-Consortium_EC-Earth3-Veg_gn_r1i1p1f1_20200919
CMCC_CMCC-ESM2_gn_r1i1p1f1_20210114
CSIRO_ACCESS-ESM1-5_gn_r1i1p1f1_20191115
E3SM-Project_E3SM-1-1-ECA_gr_r1i1p1f1_20200127
BCC_BCC-ESM1_gn_r1i1p1f1_20181129
NOAA-GFDL_GFDL-ESM4_gr_r1i1p1f1_20190726
INM_INM-CM4-8_gr1_r1i1p1f1_20190530
MPI-M_MPI-ESM1-2-HR_gn_r1i1p1f1_20190710
E3SM-Project_E3SM-1-0_gr_r1i1p1f1_20190826
MPI-M_MPI-ESM1-2-LR_gn_r1i1p1f1_20190710
AWI_AWI-CM-1-1-MR_gn_r1i1p1f1_20181218
NCAR_CESM2-WACCM-FV2_gr_r1i1p1f1_20191120
CAMS_CAMS-CSM1-0_gn_r1i1p1f1_20190708
FIO-QLNM_FIO-ESM-2-0_gn_r1i1p1f1_20191122
SNU_SAM0-UNICON_gn_r1i1p1f1_20190323
CMCC_CMCC-CM2-HR4_gn_r1i1p1f1_20200904
CAS_FGOALS-f3-L_gn_r1i1p1f1_20191007
IPSL_IPSL-CM6A-LR_gn_r1i1p1f1_20180803
AS-RCEC_TaiESM1_gn_r1i1p1f1_20200630